POLITECNICO
MILANO 1863

SCUOLA DI INGEGNERIA INDUSTRIALE
E DELL'INFORMAZIONE

A Trefftz Discontinuous Galerkin method with Absorbing Boundary Conditions for the numerical simulation of the Helmholtz problem

Tesi di Laurea Magistrale in
Mathematical Engineering - Ingegneria Matematica

Author: **Simone Pescuma**

Student ID: 962607
Advisor: Prof.ssa Paola F. Antonietti
Co-advisors: Dr. Axel Modave, Prof. Gwénaël Gabard
Academic Year: 2021-22

Je suis fort parce que je ne suis jamais dérouté par les autres et que je fais ce qui est en moi.

Paul Gauguin, 1848 - 1903

Abstract

The numerical simulation of Helmholtz problems in the time-harmonic acoustic framework set in unbounded domains requires a mesh based approach in bounded numerical domains.
Therefore, we present a Trefftz method, which is a particular Discontinuous Galerkin method, applied to the problem complemented by Absorbing Boundary Conditions.
Trefftz methods have been largely studied in the framework of Helmholtz equation and have turned out to be suitable. In particular, the use of propagative plane-waves is effective in approximating the solution. Nevertheless, their use is still limited by conditioning issues that arise whenever the approximate space becomes too large.
The combination of the wave-based Trefftz method and the relative Ultra Weak Variational Formulation with Absorbing Boundary Conditions represents a novelty that we aim at studying and investigating in the present work. It leads to a new formulation of the problem whose numerical results are exploited to evaluate the efficiency of the approach.

Keywords: Helmholtz, Trefftz, Ultra weak variational formulation, Discontinuous Galerkin, Plane waves, Absorbing boundary conditions

Sommario

La simulazione numerica dei problemi di Helmholtz nel contesto di onde acustiche tempo-periodiche in domini illimitati richiede un approccio in domini numerici limitati dotati di mesh.
Perciò, presentiamo un metodo Trefftz, che è un particolare metodo di Galerkin Discontinuo, applicato al problema complementato da Condizioni al Bordo di Assorbimento.
I metodi Trefftz sono stati ampiamenti studiati nel contesto dell'equazione di Helmholtz e sono risultati essere adatti. In particolare, l'uso di onde piane è efficace nell'approssimare la soluzione. Tuttavia, il loro uso è ancora limitato da problemi di condizionamento che sorgono ogni volta in cui lo spazio approssimante diventa troppo grande.
La combinazione del metodo Trefftz per le onde e la relativa Formulazione Variazionale Ultra Debole con Condizioni al Bordo di Assorbimento rappresenta una novità che puntiamo a studiare e investigare nel presente lavoro. Porta a una nuova formulazione del problema i cui risultati numerici sono utilizzati per valutare l'efficienza dell'approccio.

Parole chiave: Helmoltz, Trefftz, Formulazione variazionale ultra debole, Galerkin discontinuo, Onde piane, Condizioni al bordo di assorbimento

Contents

Abstract **i**

Sommario **iii**

Contents **v**

Introduction **1**

1 Helmholtz problem with Absorbing Boundary Conditions **5**
1.1 Helmholtz problem 5
1.2 Absorbing boundary conditions 7
1.2.1 Zeroth-order absorbing boundary condition 7
1.2.2 Exact absorbing boundary condition 9
1.2.3 High-order absorbing boundary condition 11
1.2.4 Dealing with corners and curved boundaries 12

2 Ultra Weak Variational Formulation with ABC **13**
2.1 Space of solutions 13
2.2 Interface conditions 14
2.3 Variational formulation 15

3 Plane-wave discretization **19**
3.1 Shape functions 19
3.2 Dealing with absorbing boundary conditions 21
3.3 Algebraic formulation 24
3.4 Theoretical and computational aspects 28
3.4.1 Convergence 28
3.4.2 Ill-conditioning 30
3.4.3 Adaptivity 31

4 Preliminary numerical study **33**
4.1 One-element benchmark 33
4.2 Study of the projection error 35
4.3 Study of the numerical error with the UWVF 38
4.3.1 Results with "full" basis 39
4.3.2 Results with adapted basis 41
4.3.3 Results with HABC 42

5 Numerical results **45**
5.1 Validation of the implementation 45
5.1.1 Validation with structured meshes 46
5.1.2 Validation with unstructured meshes 49
5.2 Study with a truncated square domain 51
5.3 Investigation with a truncated circular domain 56
5.4 Illustration of applications 60

Conclusions **63**

Bibliography **65**

List of Figures **71**

Acknowledgements **73**

Introduction

General context

The study of mechanical waves provides important information regarding the medium in which they propagate thanks to the measurement of key parameters such as velocity, amplitude and phase. The main fields of application are medical imaging, exploration of the subsurface, seismic risk assessment, electromagnetic compatibility and aeroacoustics. In this applicative contexts, numerical simulation plays a key role since it aims at replacing or at least supporting experiments and empirical studies.

In acoustics, the propagation is governed by the wave equation, which reduces to the Helmholtz equation in the frequency domain. Its solution can be retrieved by several different numerical methods. Continuous as well as Discontinuous Finite Element Methods (FEM) are among the most popular due to their robust formulations and the possibility of exploiting unstructured meshes that are convenient for the study of realistic settings and complicated geometries. Moreover, numerical techniques based on integral equations are also very popular, like the Boundary Element Method (BEM) ([1]).

In the case of standard mesh-based methods that deal with linear basis functions, the numerical solution is characterized by a specific and well-known instability called *"numerical pollution effect"*, hence several approaches have been studied in order to deal with it and limit the effect. The two main classes of methods include: local high-order polynomial methods ([2,3,4]) and wave-based methods ([5,6,7,8]), which are also known as Trefftz methods. The first one exploits the fact that the approximations due to local high-order polynomials specifically reduce the pollution, while the second one relies on the largely accepted intuition that, being the shape functions local solutions of Helmholtz equation itself, they are able to incorporate the physical characteristics of the problem, thus these methods are more able to deal with the pollution. Moreover, wave-based methods require a number of degrees of freedom that is much smaller than that required by polynomial methods ([9]).

Although most of wave propagation problems are defined in the whole space, namely an unbounded domain, numerical solutions computed with finite elements demand computational domains that are as small as possible. Hence, they are retrieved with modified problems defined on truncated domains with artificial boundaries. Even though the latter are not physical, these boundaries must be carefully modeled in order to recover the solution corresponding to the original physical problems. Hence, finite element methods must be coupled with domain truncation techniques, which simulate the outward propagation of waves at the boundary of the computational domain.

State of the art and goal of the study

Several couplings have been proposed: with exact non-local boundary conditions, local absorbing boundary conditions and perfectly matched layers. High-order Absorbing Boundary Conditions (HABCs) ([10,11,12]) and Perfectly Matched Layers (PMLs) ([13,14,15]) provide high-fidelity solutions with a limited computational cost. The ease of use of PMLs made these methods more popular than HABCs, nevertheless the parameter selection of PMLs is still tricky and depends on the discretization scheme ([16,17]), while *a priori* analysis for HABCs allows a better control on the error ([18,19]).

Moreover, the study concerning exact non-local boundary conditions has led to non-overlapping Domain Decomposition Methods (DDMs) whose transmission conditions on each interface are expressed in terms of the Dirichlet-to-Neumann (DtN) operator ([20, 21, 22, 23, 24, 25]). In addition, there exist also several studies concerning alternative Discontinuous Galerkin methods with hybridization and characteristic variables ([26, 27, 28]) that include techniques regarding Absorbing Boundary Conditions and Perfectly Matched Layers.

The goal of this study is to investigate the behaviour of numerical solutions obtained by a Trefftz method coupled with proper ABCs in the context of rectangular domains and domains with curved boundaries and to study its efficiency.

Environment of the internship/PhD

The present report aims at describing the main results I obtained during my internship in POEMS from April 1st 2022 to August 31st 2022 and beginning of PhD from October 1st 2022 to December 31st 2022 both supervised by Axel Modave and Gwénaël Gabard. The lab, whose name is a French acronym that, in English, stands for *Wave Propagation: Mathematical Study and Simulation*, is a mixed research unit which was founded in 2005 and whose three parent institutions are CNRS, ENSTA Paris and Inria. The unit is located at ENSTA Paris, in the campus of Institut Polytechnique de Paris, Palaiseau, France. POEMS scientific activities are devoted to the development of mathematical and numerical studies about wave propagation, in all domains of physics and mechanics, namely electromagnetic, acoustic, elastic and gravitational waves. Its work concerns the modelling of complex problems, the mathematical analysis of these models, the development of approximation methods and of computational codes.

Code

The majority of my study was focused on coding a finite element method through MATLAB for the core part, that is the numerical solver, and the software GMSH for generating the meshes. In particular, I personally took care of all the code, except for the functions in charge of computing the numerical error and plotting the exact and numerical solutions, which were kindly provided to me respectively by Axel Modave and Gwénaël Gabard, who also helped me checking the code and analysing the results. I developed a first version of the code to validate it, then I proceeded with a deeper analysis.

Structure of the thesis

In Chapter 1 we introduce the Helmholtz problem, focusing on the meaning of the Absorbing Boundary Conditions (ABCs), its continuous formulation and approximations.

In Chapter 2 we present the Trefftz method and we exhibit the concept of Ultra Weak Variational Formulation (UWVF) applied to the problem with ABCs.

In Chapter 3 we describe the discretized problem corresponding to the UWVF with ABC.

In Chapter 4 we study the numerical method with an elementary example in which the numerical domain is composed by one single element.

In Chapter 5 we provide numerical results and analysis exploiting several different benchmarks with numerical domains equipped with meshes in order to validate the code and enlighten main advantages and issues of the scheme.

1 | Helmholtz problem with Absorbing Boundary Conditions

The goal of this chapter is to introduce the Helmholtz equation supplemented by suitable absorbing boundary conditions, explaining their physical meaning and present their high-order approximation.

1.1. Helmholtz problem

As we quickly said in the introduction, Helmholtz equation is the expression of the wave equation in the frequency domain. Let us show how, starting from the wave equation in the time domain, we get its expression in the frequency domain. Let us consider the scalar wave equation

$$\frac{\partial^2}{\partial t^2} v(t, \boldsymbol{x}) = c^2(\boldsymbol{x}) \Delta v(t, \boldsymbol{x}) + F(t, \boldsymbol{x}),$$

where v is the amplitude of the time-harmonic wave, c is the local speed of propagation of the wave and F is the source term. Let us suppose we look for solutions with a single angular time frequency ω and that the waves and the source are of the form

$$v(t, \boldsymbol{x}) = u(\boldsymbol{x}) e^{-\imath \omega t}, \qquad F(t, \boldsymbol{x}) = g(\boldsymbol{x}) e^{-\imath \omega t}.$$

Plugging these two expressions into the wave equation, we have

$$-\omega^2 u(\boldsymbol{x}) e^{-\imath \omega t} = c^2(\boldsymbol{x}) \Delta u(\boldsymbol{x}) e^{-\imath \omega t} + g(\boldsymbol{x}) e^{-\imath \omega t},$$

which reduces to

$$\Delta u(\boldsymbol{x}) + \frac{\omega^2}{c^2(\boldsymbol{x})} u(\boldsymbol{x}) = -\frac{g(\boldsymbol{x})}{c^2(\boldsymbol{x})}.$$

Finally, defining the wave number $\kappa(\boldsymbol{x}) = \omega/c(\boldsymbol{x})$ and the source $f(\boldsymbol{x}) = -g(\boldsymbol{x})/c^2(\boldsymbol{x})$, we get the final expression of Helmholtz equation

$$\Delta u + \kappa^2 u = f.$$

From now on, the source term is taken null, that is $f = 0$. As a final remark, Helmholtz equation can be thought as a steady state version of the wave equation though, of course, just the amplitude is steady, not the oscillating factor $e^{-\imath\omega t}$.

We now introduce the sound-hard scattering problem. Let $D \subset \mathbb{R}^n$, $n = 2, 3$ be a bounded domain that represents an impenetrable object with boundary Γ. We denote by Ω the complement of D, namely $\Omega = \mathbb{R}^n \backslash \overline{D}$, that represents the exterior isotropic domain where D is embedded. An incident plane-wave u^{inc} that illuminates the scatterer D generates a diffracted acoustic field $u : \Omega \to \mathbb{C}$ that satisfies the following exterior boundary-value problem

$$\begin{cases} \Delta u + \kappa^2 u = 0, & \boldsymbol{x} \in \Omega, \\ \partial_{\boldsymbol{n}} u = g, & \boldsymbol{x} \in \Gamma, \\ \lim\limits_{|\boldsymbol{x}|\to\infty} |\boldsymbol{x}|^{\frac{n-1}{2}} \left(\nabla u \cdot \dfrac{\boldsymbol{x}}{|\boldsymbol{x}|} - \imath\kappa u \right) = 0, \end{cases} \tag{1.1.1}$$

where $\boldsymbol{n}$ is the outward unit normal on the boundary of Ω and $g = -\partial_{\boldsymbol{n}} u^{\text{inc}}$. The Sommerfeld radiation condition at infinity is imposed to ensure the uniqueness of the solution.

Let us recall that whenever the domain is infinite or too large to discretize numerically, Absorbing Boundary Conditions (ABCs) need to be considered. The domain is cut down to a manageable size, its artificial external boundary Γ_{ext} is introduced and the ABCs are applied to it. Hence, the new boundary Γ_{ext} models the effect of the rest of the domain. Moreover, Helmholtz equation needs to be supplemented by boundary conditions such as Dirichlet, Neumann or Robin on the remaining part of the boundary, that is Γ_{int}.

For simplicity, from now on we limit ourselves to a 2D reference case. However, the whole study extends to the 3D case in a straightforward way. Let $\Omega \subset \mathbb{R}^2$ be a domain represented in Fig. 1.1. We consider the following model boundary-value problem set in terms of Helmholtz equation for $u : \Omega \to \mathbb{C}$

$$\begin{cases} \Delta u + \kappa^2 u = 0, & \boldsymbol{x} \in \Omega, \\ \partial_{\boldsymbol{n}} u = g, & \boldsymbol{x} \in \Gamma_{\text{int}}, \\ \partial_{\boldsymbol{n}} u = \mathcal{B} u, & \boldsymbol{x} \in \Gamma_{\text{ext}}, \end{cases} \tag{1.1.2}$$

where Γ_{ext} stands for the external boundary of Ω, Γ_{int} for its complementary, so that $\partial\Omega = \Gamma_{\text{ext}} \cup \Gamma_{\text{int}}$, $\boldsymbol{n}$ is the outward unit normal on the boundary of Ω and $\mathcal{B}$ is a suitable Dirichlet-to-Neumann (DtN) operator that permits to model absorption on Γ_{ext} and that we will characterize in details in the next section.

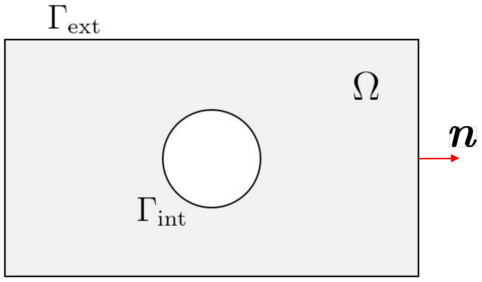

Figure 1.1: Example of domain with rectangular artificial external boundary.

1.2. Absorbing boundary conditions

The reduced problem (1.1.2) should have the same solutions as those of the full one (1.1.1) restricted to the smaller domain Ω. In the context of waves, this means that the ABCs are to be implemented so that all outgoing waves are allowed to pass the artificial boundary unaffected, in particular without being reflected, while no incoming wave is allowed into the domain from outside.

In order to understand the meaning and retrieve the boundary condition of problem (1.1.2), which is equivalent to characterize the operator $\mathcal{B}$, we first restrict ourselves to the one-dimensional case. The same reasoning can be easily extended to the multidimensional one, as we do in the final part of this section.

1.2.1. Zeroth-order absorbing boundary condition

First, we introduce the most simple ABC, namely the Zeroth-order Absorbing Boundary Condition (ABC0). To begin, we consider the non-homogeneous Helmholtz equation in a one-dimensional and bounded domain $\Omega = (0, L)$

$$u_{xx} + \kappa^2 u = f, \quad x \in \Omega,$$

and let us suppose that $f(x)$ is compactly supported on Ω.

We want to derive the ABC0 for $x = 0$ and $x = L$. Let us start observing that for $x = 0$, f is identically zero, hence $u(x)$ solves

$$u_{xx} + \kappa^2 u = 0, \quad x = 0.$$

By linearity, we can write the solution of the equation as linear combination of the fundamental solutions of the equation, that is two waves moving in opposite directions

$$u(x) = \alpha e^{-\imath\kappa x} + \beta e^{\imath\kappa x}, \quad x = 0, \tag{1.2.1}$$

where, because of the time-dependency convention with $e^{-\imath\kappa t}$, $\alpha e^{-\imath\kappa x}$ propagates towards the left of the domain and $\beta e^{\imath\kappa x}$ towards the right. We want the ABC to accept any value of α, but disallow a non-zero β. We note that

$$u_x + \imath\kappa u = -\alpha\imath\kappa e^{-\imath\kappa x} + \beta\imath\kappa e^{\imath\kappa x} + \alpha\imath\kappa e^{-\imath\kappa x} + \beta\imath\kappa e^{\imath\kappa x} = 2\beta\imath\kappa e^{\imath\kappa x}.$$

Applying this at $x = 0$ and setting $\beta = 0$, we get

$$u_x + \imath\kappa u = 0, \quad x = 0.$$

Similarly, at $x = L$ the boundary condition should force $\alpha = 0$ and accept any β. Proceeding as above, we get

$$u_x - \imath\kappa u = 0, \quad x = L.$$

Notice that above the waves are generated by the source $f(x)$. Sometimes, rather than a source, an incoming wave from infinity is considered, for instance in scattering problems. The boundary condition should then both model this incoming wave and act as an absorbing boundary condition, while $f(x)$ is set to zero. The result is an non-homogeneous version of the ABC. For instance, if the incoming wave has amplitude A, instead of setting β to zero in the previous computations, we should set it to A. Applying it at $x = 0$, it gives the non-homogeneous boundary condition

$$u_x + \imath\kappa u = 2\imath\kappa A, \quad x = 0.$$

In higher dimensions there is no a simple form like (1.2.1) for the solution close to the artificial boundary. In general, there will be waves propagating in every direction at each boundary point. An exact absorbing boundary condition of the type we derived in one dimension must therefore necessarily be non-local, *e.g.* expressed via an integral over the boundary. Applying such non-local conditions numerically is expensive. Instead, it is preferred to use various local approximation of the ABC. Since they are not exact, they will in general cause spurious reflected waves when a wave hits the artificial boundary.

One common approach is to assume that the solution of the full problem, close to the artificial boundary, can be approximated by a plane wave that propagates in a direction normal to the boundary. Then the same argument as in one dimension can be used. Indeed, if

$$u(x) \approx Ce^{\imath\kappa \boldsymbol{n}\cdot\boldsymbol{x}},$$

where $\boldsymbol{n}$ is the normal of the boundary, then

$$\partial_{\boldsymbol{n}} u - \imath\kappa u \approx \imath\kappa C e^{\imath\kappa \boldsymbol{n}\cdot\boldsymbol{x}} \partial_{\boldsymbol{n}}(\boldsymbol{n}\cdot\boldsymbol{x}) - \imath\kappa C e^{\imath\kappa \boldsymbol{n}\cdot\boldsymbol{x}} \approx 0.$$

This motivates the simplest ABC, that takes the form

$$\partial_{\boldsymbol{n}} u - \imath\kappa u = 0, \quad \boldsymbol{x} \in \partial\Omega. \tag{1.2.2}$$

As a final remark, we observe that when a plane wave hits the boundary at an oblique angle with direction $\boldsymbol{k} \neq \boldsymbol{n}$, ABC (1.2.2) gives an error, because of the artificially reflected wave, whose size is proportional to the difference $|\boldsymbol{k}-\boldsymbol{n}|$ for small deviations. It is possible to also derive higher order ABCs in this difference, which produce much smaller artificial reflections and this is the main goal of the following sections.

1.2.2. Exact absorbing boundary condition

In this section, we derive the exact absorbing boundary condition for a straight boundary. The method we analyze is based on the work presented in [29] and later exploited in [30].

We consider Helmholtz problem in the whole 2D-space, that is

$$\Delta u + \kappa^2 u = f, \quad \boldsymbol{x} \in \mathbb{R}^2.$$

We decompose the unbounded domain $\mathbb{R}^2$ into the union of the two semi-planes: the interior region $\Omega = \{(x, y) \in \mathbb{R}^2 : x < 0\}$ and the exterior region $\Omega^{\text{ext}} = \{(x, y) \in \mathbb{R}^2 : x > 0\}$ separated by the plane interface Γ whose equation is $x = 0$. The exterior medium is assumed to be homogeneous, that is κ is constant in Ω^{ext}, and free of source, that is f is compactly supported on Ω. The goal is to prescribe a boundary condition on Γ which is able to represent the outward propagation of waves leaving Ω.

We use the classical approach to obtain the exact non-reflecting boundary condition, which is to solve the exterior Helmholtz problem defined in Ω^{ext} for some Dirichlet data $\overline{u}(y)$ on Γ. Applying the multidimensional transverse Fourier transform $\mathcal{F}_y$ in the y-direction to the Helmholtz equation yields

$$(\partial_x^2 + \lambda_+\lambda_-)\mathcal{F}_y[u](x, \xi_y) = 0, \text{ for } x > 0, \xi_y \in \mathbb{R},$$

where ξ_y is the dual variable of y in the Fourier space and $\lambda_\pm$ is such that

$$\lambda_\pm(\xi_y) = \mp\sqrt{\kappa^2 - \xi_y^2}.$$

The solution that contains only outgoing traveling modes and bounded evanescent modes reads

$$\mathcal{F}_y[u](x, \xi_y) = \mathcal{F}_y[\overline{u}](\xi_y)e^{x\lambda_+(\xi_y)}.$$

Taking the derivative in x of this solution leads to

$$\partial_x\mathcal{F}_y[u](x, \xi_y) = \lambda_+(\xi_y)\mathcal{F}_y[u](x, \xi_y),$$

and then, using the inverse Fourier transform $\mathcal{F}_y^{-1}$, we have

$$\partial_x u(x, y) = \mathcal{F}_y^{-1}[\lambda_+(\xi_y)\mathcal{F}_y[u](x, \xi_y)].$$

Taking the restriction on Γ gives the exact non-reflective boundary condition for the interior problem,

$$\partial_x u = \mathcal{B}u, \quad \boldsymbol{x} \in \Gamma,$$

where $\mathcal{B}$ is the pseudo-differential operator defined as

$$\mathcal{B} = \mathcal{F}_y^{-1}[\lambda_+(\xi_y)\mathcal{F}_y] = \imath\kappa\sqrt{1 + \partial_{yy}/\kappa^2}.$$

The operator $\mathcal{B}$ is the exact Dirichlet-to-Neumann (DtN) operator for this problem.

The latter can be rewritten as follows in the more general case of outward unit normal $\boldsymbol{n}$ on Γ: the exact absorbing boundary condition becomes

$$\partial_{\boldsymbol{n}} u = \mathcal{B} u, \quad \boldsymbol{x} \in \Gamma, \tag{1.2.3}$$

with the pseudo-differential operator $\mathcal{B}$ and the Laplace-Beltrami operator Δ_Γ defined as

$$\mathcal{B} = \imath\kappa\sqrt{1 + \Delta_\Gamma/\kappa^2}, \qquad \Delta_\Gamma = \Delta - \partial_{\boldsymbol{nn}}. \tag{1.2.4}$$

1.2.3. High-order absorbing boundary condition

Boundary condition (1.2.3) is non-local because of the square root in the symbol of $\mathcal{B}$ and this leads to issues whenever a finite element solver is exploited because of a strong coupling of the unknowns defined onto the fictitious boundary and thus a dense block in the matrix of the linear system for the associated entries. Nevertheless, local high-order boundary conditions can be derived by approximating the square root in (1.2.4).

In [29], using a Padé approximation of the square root, a family of local boundary conditions is derived. In particular, the $(2N+1)$th-order Padé approximation of the square root $f(X) = \sqrt{1+X}$ is written as the rational function

$$f^{\text{Padé}}_{2N+1}(X) = 1 + \frac{2}{M}\sum_{n=1}^{N} c_n \left(1 - \frac{c_n + 1}{c_n + 1 + X}\right),$$

with $c_n = \tan^2(n\pi/M)$ and $M = 2N+1$. Nevertheless, Padé approximations lead to boundary conditions that are inappropriate for evanescent modes and inaccurate for grazing waves. In [31], a modified approximation with a change of variable to rotate the branch cut of the square root by some angle ϕ is proposed and leads to

$$f^{\phi}_{2N+1}(X) = e^{\imath\phi/2} f^{\text{Padé}}_{2N+1}(e^{-\imath\phi}(1+X) - 1) = e^{\imath\phi/2}\left[1 + \frac{2}{M}\sum_{n=1}^{N} c_n \left(1 - \frac{e^{\imath\phi}(c_n+1)}{(e^{\imath\phi}c_n + 1) + X}\right)\right]. \tag{1.2.5}$$

The latter highly improves the accuracy of the HABC for evanescent modes, while it slightly increases the reflection of traveling modes. Letting the angle ϕ grow, the effect results in being more evident, as it is highlighted in [32].

There exist more general approximations of the DtN operator. In particular, Higdon-type HABCs ([33]) turned out to be exact for waves that propagate with any angle of incidence of a given set $\{\theta_m\}_{m=1,\dots,M}$, but they keep on being inefficient for evanescent waves. Nevertheless, Complete Radiation Boundary Conditions (CRBCs) ([34]) are able to deal with both propagative and evanescent waves.

Combining approximation (1.2.5) with the pseudo-differential operator (1.2.4), we have the approximate boundary condition

$$\partial_{\boldsymbol{n}} u = \mathcal{R} u, \quad \boldsymbol{x} \in \Gamma, \tag{1.2.6}$$

where $\mathcal{R}$ is the pseudo-differential operator defined as

$$\mathcal{R} = \imath\kappa e^{\imath\phi/2}\left[1 + \frac{2}{M}\sum_{n=1}^{N} c_n \left(1 - \frac{e^{\imath\phi}(c_n+1)}{(e^{\imath\phi}c_n+1) + \Delta_\Gamma/\kappa^2}\right)\right]. \tag{1.2.7}$$

1.2.4. Dealing with corners and curved boundaries

The ABC we derived in Section 1.2.2 is suitable only for planar boundaries since it consists in a non-local boundary condition expressed in terms of the DtN operator which is exact only for planar boundaries.

In the case of a polygonal domain, that is a domain with straight sides and corners, a special treatment that deals with the local non-regularity of the boundary in the areas of the corners may be required ([30]).

In [35], a modified form of the ABC which is suitable for regular curved boundaries is retrieved. In two dimensions, the modified ABC for a regular planar curve $\Gamma \subset \mathbb{R}^2$ reads

$$\partial_{\boldsymbol{n}} u = (\mathcal{B} + \mathcal{S}) u, \quad \boldsymbol{x} \in \Gamma, \tag{1.2.8}$$

where $\mathcal{S}$ is the differential operator defined as

$$\mathcal{S} = -\frac{\gamma}{2} + \frac{\gamma^2}{8(\gamma - i\kappa)} - \partial_{\boldsymbol{t}}\left(\frac{\gamma}{2\kappa^2}\partial_{\boldsymbol{t}}\right), \tag{1.2.9}$$

where γ is the local curvature which is defined as $\gamma = 1/\rho$, with ρ the radius of curvature that is the radius of the osculating circle.

2 | Ultra Weak Variational Formulation with ABC

In order to carry out the calculation of the numerical solution of Helmholtz problem, we proceed in the standard way, hence we start with the first key step, that is writing its variational formulation. The use of the Ultra Weak Variational Formulation, which is a special Discontinuous Galerkin method that belongs to the class of wave-based/Trefftz methods, combined with High-order Absorbing Boundary Conditions represents a novelty that has never been studied before.

2.1. Space of solutions

The key idea of Trefftz methods is to include *a priori* knowledge about the local behaviour of the solution into the numerical method. This aim is achieved by considering an approximation basis V composed by local canonical solutions of the equation. It is generally assumed that Treffz methods allow better accuracy than non-Treffz methods, since in the second case their approximation basis does not embed any physical feature and is not related to the equation itself. Nevertheless, the comparison between high-order polynomial finite element methods and wave-based methods is still an open discussion ([9]) and several studies are still being carried on.

In the context of Helmholtz problem, considering a non-overlapping triangulation $\mathcal{T}$ composed by K elements T_i with $i = 1, ..., K$, we take the approximation space

$$V = \prod_{i=1}^{K} \{v_i \in H^1(T_i) : \Delta v_i + \kappa^2 v_i = 0\}. \tag{2.1.1}$$

In our work, we will consider a set of P plane waves as basis functions for each element, though other sets can be chosen such as Green or Bessel functions ([6,8]).

2.2. Interface conditions

Local solutions of the Helmholtz equation u_i in an element $T_i \in \mathcal{T}$ and u_j in its neighboring element $T_j \in \mathcal{T}$ have to satisfy the following conditions

$$u_i = u_j, \quad \boldsymbol{x} \in F_{ij}, \tag{2.2.1}$$

$$\partial_{\boldsymbol{n}_i} u_i + \partial_{\boldsymbol{n}_j} u_j = 0, \quad \boldsymbol{x} \in F_{ij}, \tag{2.2.2}$$

where $\boldsymbol{n}_i$ denotes the outward unit normal on the boundary ∂T_i of $\overline{T_i}$, u_i denotes the restriction of u on T_i, *i.e.* $u_i = u|_{T_i}$, and $\overline{F}_{ij} = \partial\overline{T}_i \cap \partial\overline{T}_j$ denotes each edge shared by an element T_i and an element T_j of $\mathcal{T}$, as it is shown in Fig. 2.1. Notice that the previous conditions guarantee the continuity of the acoustic pressure and normal particle velocity, respectively, across the interfaces of the elements.

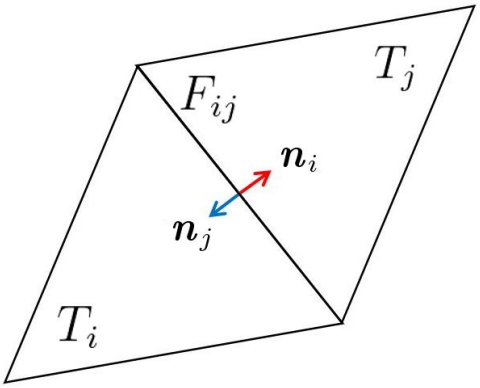

Figure 2.1: Notation: two adjacent triangular elements $T_i, T_j \in \mathcal{T}$.

The matching conditions on the interfaces and the boundary conditions are variationally expressed in terms of proper outgoing and incoming traces that need to be defined. Let us proceed by introducing the concept of outgoing and incoming trace, hence we give the definition of outgoing operator $\mathcal{O}_i$ and incoming operator $\mathcal{I}_i$ that need to be applied to a function u_i in order to retrieve, respectively, its outgoing and incoming trace on the boundary ∂T_i of any element $T_i \in \mathcal{T}$

$$\mathcal{O}_i = \frac{1}{2}\left(\frac{1}{\imath\kappa}\frac{\partial}{\partial \boldsymbol{n}_i} + 1\right),$$

$$\mathcal{I}_i = \frac{1}{2}\left(-\frac{1}{\imath\kappa}\frac{\partial}{\partial \boldsymbol{n}_i} + 1\right).$$

As we will underline later, these two operators require a minimum regularity of the local solution which they are applied to so that $\mathcal{O}_i u_i, \mathcal{I}_i u_i \in L^2(\partial T_i)$ and all the integrals that will appear in the variational formulation are well defined. Thus, they are such that $\mathcal{O}_i u_i, \mathcal{I}_i u_i : L^2(\partial T_i) \to L^2(\partial T_i)$.

Let us observe that conditions (2.2.1) and (2.2.2) can be equivalently written in terms of outgoing traces as

$$\mathcal{O}_i u_i = \mathcal{O}_i u_j,$$
$$\mathcal{O}_j u_i = \mathcal{O}_j u_j.$$

In order to understand the meaning of the outgoing and incoming trace, we follow the example presented in [36], hence we consider a superposition of two plane waves $\alpha_i^+ \exp(+\imath\kappa \boldsymbol{x} \cdot \boldsymbol{n}_i)$ and $\alpha_i^- \exp(-\imath\kappa \boldsymbol{x} \cdot \boldsymbol{n}_i)$ propagating at normal incidence to an edge F of ∂T_i

$$v_i(\boldsymbol{x}) = \alpha_i^+ \exp(+\imath\kappa \boldsymbol{x} \cdot \boldsymbol{n}_i) + \alpha_i^- \exp(-\imath\kappa \boldsymbol{x} \cdot \boldsymbol{n}_i).$$

The two plane waves are respectively propagating towards the exterior and the interior of T_i. The outgoing and incoming traces

$$\mathcal{O}_i v_i = \frac{1}{2}\left(\frac{1}{\imath\kappa}\frac{\partial v_i}{\partial \boldsymbol{n}_i} + v_i\right) = \alpha_i^+ \exp(+\imath\kappa \boldsymbol{x} \cdot \boldsymbol{n}_i),$$

$$\mathcal{I}_i v_i = \frac{1}{2}\left(-\frac{1}{\imath\kappa}\frac{\partial v_i}{\partial \boldsymbol{n}_i} + v_i\right) = \alpha_i^- \exp(-\imath\kappa \boldsymbol{x} \cdot \boldsymbol{n}_i),$$

exactly coincide with respectively the trace of the outgoing wave and the one of the incoming wave through the edge F of T_i. This fact justifies the terminology we use.

2.3. Variational formulation

Now we have all the elements that are necessary to state and prove the main result of this section. Let us underline the fact that the theorem that follows was proved for the first time in [37] in the case of the Helmholtz problem coupled by a zeroth-order absorbing boundary condition. Here, we extend this formulation and the related proof to the more general case of Helmholtz problem coupled with any kind of absorbing boundary condition.

Theorem 2.1 (Ultra-Weak Variational Formulation):
Let Ω be a bounded domain and $\mathcal{T}$ one of its non-overlapping partitions composed by triangular elements T_i, with $i = 1, ..., K$ where K is the number of elements. Let the solution $u \in H^1(\Omega)$ of problem (1.1.2) be regular enough in Ω, that is all its required derivatives are in $L^2(\partial T_i)$ for any $i = 1, ..., K$ and let V as in (2.1.1). Then, $\forall v \in V$, the solution u satisfies

$$\sum_i \int_{\partial T_i} \frac{1}{2}\left(\frac{1}{\imath\kappa}\frac{\partial u_i}{\partial \boldsymbol{n}_i} + u_i\right)\overline{\frac{1}{2}\left(\frac{1}{\imath\kappa}\frac{\partial v_i}{\partial \boldsymbol{n}_i} + v_i\right)} - \sum_i \int_{\Gamma_i^{\text{ext}}} -\frac{1}{2\imath\kappa}\mathcal{B}u_i\overline{\frac{1}{2}\left(-\frac{1}{\imath\kappa}\frac{\partial v_i}{\partial \boldsymbol{n}_i} + v_i\right)}$$

$$-\sum_i \sum_{j\neq i} \int_{F_{ij}} \frac{1}{2}\left(\frac{1}{\imath\kappa}\frac{\partial u_j}{\partial \boldsymbol{n}_j} + u_j\right)\overline{\frac{1}{2}\left(-\frac{1}{\imath\kappa}\frac{\partial v_i}{\partial \boldsymbol{n}_i} + v_i\right)} - \sum_i \int_{\Gamma_i} \frac{1}{2}u_i\overline{\frac{1}{2}\left(-\frac{1}{\imath\kappa}\frac{\partial v_i}{\partial \boldsymbol{n}_i} + v_i\right)}$$

$$= \sum_i \int_{\Gamma_i^{\text{int}}} -\frac{1}{2\imath\kappa} g\overline{\frac{1}{2}\left(-\frac{1}{\imath\kappa}\frac{\partial v_i}{\partial \boldsymbol{n}_i} + v_i\right)}. \tag{2.3.1}$$

Proof.

Taking into account the Helmholtz problem (1.1.2) and the functional space for test functions (2.1.1), we have

$$\begin{cases} \Delta u + \kappa^2 u = 0, & \boldsymbol{x} \in \Omega, \\ \Delta\overline{v_i} + \kappa^2\overline{v_i} = 0, & \boldsymbol{x} \in T_i, \end{cases} \tag{2.3.2}$$

for any $T_i \in \mathcal{T}$ and for any $v \in V$. Integrating by parts in (2.3.2), we have

$$\begin{cases} \displaystyle\int_{T_i} (-\nabla u_i\overline{\nabla v_i} + \kappa^2 u_i\overline{v_i}) = -\int_{\partial T_i} \overline{v_i}\partial_{\boldsymbol{n}_i}u_i, \\ \displaystyle\int_{T_i} (-\nabla u_i\overline{\nabla v_i} + \kappa^2 u_i\overline{v_i}) = -\int_{\partial T_i} u_i\overline{\partial_{\boldsymbol{n}_i}v_i}, \end{cases}$$

that gives

$$\int_{\partial T_i}\left(u_i\overline{\frac{\partial v_i}{\partial \boldsymbol{n}_i}} - \frac{\partial u_i}{\partial \boldsymbol{n}_i}\overline{v_i}\right) = 0.$$

This fact can be exploited here below

$$\int_{\partial T_i} \frac{1}{2}\left(\frac{1}{\imath\kappa}\frac{\partial u_i}{\partial \boldsymbol{n}_i} + u_i\right)\overline{\frac{1}{2}\left(\frac{1}{\imath\kappa}\frac{\partial v_i}{\partial \boldsymbol{n}_i} + v_i\right)} - \int_{\partial T} \frac{1}{2}\left(-\frac{1}{\imath\kappa}\frac{\partial u_i}{\partial \boldsymbol{n}_i} + u_i\right)\overline{\frac{1}{2}\left(-\frac{1}{\imath\kappa}\frac{\partial v_i}{\partial \boldsymbol{n}_i} + v_i\right)}$$

$$= -\frac{1}{2\imath\kappa}\int_{\partial T_i}\left(u_i\overline{\frac{\partial v_i}{\partial \boldsymbol{n}_i}} - \frac{\partial u_i}{\partial \boldsymbol{n}_i}\overline{v_i}\right) = 0.$$

The continuity of u on F_{ij} and the boundary conditions of system (1.1.2) write

$$\begin{cases} \frac{1}{2}\left(-\frac{1}{\imath\kappa}\partial_{\boldsymbol{n}_i}+1\right)u_i = \frac{1}{2}\left(\frac{1}{\imath\kappa}\partial_{\boldsymbol{n}_j}+1\right)u_j, & \boldsymbol{x}\in F_{ij}, \\ \partial_{\boldsymbol{n}_i}u_i = \mathcal{B}u_i, & \boldsymbol{x}\in\Gamma_i^{\text{ext}} = \partial T_i\cap\Gamma_{\text{ext}}, \\ \partial_{\boldsymbol{n}_i}u_i = g, & \boldsymbol{x}\in\Gamma_i^{\text{int}} = \partial T_i\cap\Gamma_{\text{int}}. \end{cases}$$

Let us sum over all the elements and let us exploit the previous relations

$$\sum_i\int_{\partial T_i}\frac{1}{2}\left(\frac{1}{\imath\kappa}\frac{\partial u_i}{\partial \boldsymbol{n}_i}+u_i\right)\overline{\frac{1}{2}\left(\frac{1}{\imath\kappa}\frac{\partial v_i}{\partial \boldsymbol{n}_i}+v_i\right)} - \sum_i\int_{\Gamma_i^{\text{ext}}}-\frac{1}{2\imath\kappa}\mathcal{B}u_i\overline{\frac{1}{2}\left(-\frac{1}{\imath\kappa}\frac{\partial v_i}{\partial \boldsymbol{n}_i}+v_i\right)}$$

$$-\sum_i\sum_{j\neq i}\int_{F_{ij}}\frac{1}{2}\left(\frac{1}{\imath\kappa}\frac{\partial u_j}{\partial \boldsymbol{n}_j}+u_j\right)\overline{\frac{1}{2}\left(-\frac{1}{\imath\kappa}\frac{\partial v_i}{\partial \boldsymbol{n}_i}+v_i\right)} - \sum_i\int_{\Gamma_i}\frac{1}{2}u_i\overline{\frac{1}{2}\left(-\frac{1}{\imath\kappa}\frac{\partial v_i}{\partial \boldsymbol{n}_i}+v_i\right)}$$

$$= \sum_i\int_{\Gamma_i^{\text{int}}}-\frac{1}{2\imath\kappa}g\overline{\frac{1}{2}\left(-\frac{1}{\imath\kappa}\frac{\partial v_i}{\partial \boldsymbol{n}_i}+v_i\right)}.$$

□

Let us remark once again that the formulation that we have just presented is a generalisation of the one shown in [37]. Indeed the DtN operator that we have exploited is a generalization of $\mathcal{B} = \imath\kappa$.

3 | Plane-wave discretization

Here we deal with the second and final step of the theoretical presentation, which consists in the discretization of the Ultra-Weak Variational Formulation that we presented in the previous chapter. In particular, we focus on the discretization of the terms that approximate the ABC that we presented in Section 1.2.

3.1. Shape functions

Taking back the notation of [36], we apply the Galerkin wave-based method considering a plane-wave basis, that is

$$\{v_{\boldsymbol{d}_p}\}_{1\leq p\leq P}, \quad v_{\boldsymbol{d}_p}(\boldsymbol{x}) = \exp(\imath\kappa \boldsymbol{d}_p \cdot \boldsymbol{x}),$$

where $\boldsymbol{d}_p$ with $p = 1, ..., P$ belongs to a finite subset

$$\mathbb{S}_2^P = \{\boldsymbol{d}_1, ..., \boldsymbol{d}_P\},$$

consisting of P different directions of the unit circle $\mathbb{S}_2$ of $\mathbb{R}^2$ and $\boldsymbol{x}$ is a generic point of the plane. The parameter P refers to the number of plane waves used in each $T_i \in \mathcal{T}$. *A priori* it can be different for each element T_i, but we will use a fixed number of plane waves P for each element T_i of the triangulation $\mathcal{T}$ without loss of generality.

Thus, the solution in T_i has the following discretized form

$$u_i^P = \sum_{p=1}^{P} \alpha_{T_i,\boldsymbol{d}_p} v_{\boldsymbol{d}_p}, \tag{3.1.1}$$

where $\alpha_{T_i,\mathbf{d}_p} \in \mathbb{C}$ are the coefficients of the linear combination of the plane-wave basis elements.

It is important to highlight once again the fact that on each element T_i of the triangulation $\mathcal{T}$ we can define a different set of shape functions, which means that the cardinality P of the set may be different, as well as the way the directions are distributed over $\mathbb{S}_2$. This is an important aspect whose potential will be discussed later in this section and partially exploited in some of the numerical simulations. Indeed, it is possible to exploit this property to select elementwise the best set of shape functions according to criteria that need to be chosen with respect to the properties of the numerical solution itself and the problem we aim at numerically solving.

Finally, for the moment, we consider a system of directions for the plane-wave basis uniformly distributed over $\mathbb{S}_2$

$$\boldsymbol{d}_p = (\cos\theta_p, \sin\theta_p), \quad \theta_p = \theta_1 + (p-1)(2\pi/P), \quad p = 1, ..., P,$$

with a number P of directions. The first angle θ_1 is called *shift* in the sequel. An example is shown in Fig. 3.1.

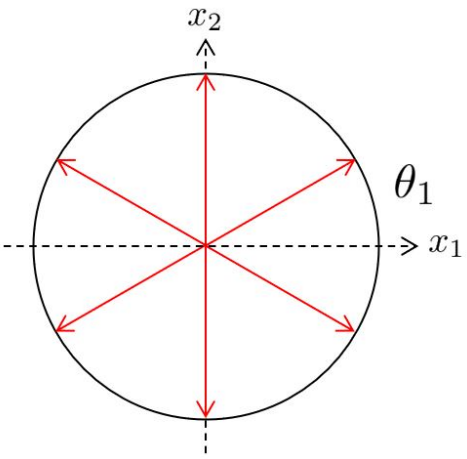

Figure 3.1: Example of $P = 6$ uniformly spaced directions, with $\theta_1 = \pi/6$.

3.2. Dealing with absorbing boundary conditions

Dealing with the discretization of formulation (2.3.1), we have to take care of the operator $\mathcal{B}$. We display the discretized forms of its approximations as presented in Chapter 1.

- $\imath\kappa$:

it simply consists in the zeroth-order ABC (1.2.2), namely

$$\mathcal{B} = \imath\kappa. \tag{3.2.1}$$

- sqrt:

a fundamental and crucial aspect that characterizes the use of plane-waves in the Trefftz method is that, unlike the use of polynomials, it lets us avoid the problem concerning the approximation of the operator $\mathcal{B}$: indeed, it is possible to exactly compute it. Let us recall (1.2.3) and (1.2.4) which have to be verified by the exact solution $u^{\text{ex}} = e^{\imath\kappa\widehat{\boldsymbol{d}}\cdot\boldsymbol{x}}$.

$$\frac{\partial u^{ex}}{\partial \boldsymbol{n}} = \nabla u^{ex} \cdot \boldsymbol{n} = \imath\kappa(\widehat{\boldsymbol{d}} \cdot \boldsymbol{n})u^{ex},$$

$$\mathcal{B}u^{ex} = \imath\kappa\sqrt{1 + \frac{\Delta_\Gamma}{\kappa^2}}u^{ex},$$

whose comparison let us retrieve that

$$\sqrt{1 + \frac{\Delta_\Gamma}{\kappa^2}} = (\widehat{\boldsymbol{d}} \cdot \boldsymbol{n}).$$

Because of the positivity forced by the left hand side of the previous equation, we deduce that the latter, in order to hold true, needs to present a positive right hand side as well, that is $(\widehat{\boldsymbol{d}}\cdot\boldsymbol{n}) \geq 0$, which is satisfied whenever the exact solution is outgoing. The previous consideration turns out to be crucial because an ABC is prescribed onto the portions of the boundary $\partial\Omega$ for which there is an *a priori* knowledge concerning the direction of the exact solution, which specifically needs to be outgoing. Therefore, in terms of discretizion, an ABC is equivalent to prescribing a non homogeneous Neumann boundary condition that holds true only for those plane-waves of the basis that are outgoing. Further manipulating the equation, we get to the final expression of the Laplace-Beltrami operator as application to plane-waves $u_p = e^{\imath\kappa\boldsymbol{d}_p\cdot\boldsymbol{x}}$, $p = 1, ..., P$, that is

$$\Delta_\Gamma = -\kappa^2(1 - (\boldsymbol{d}_p \cdot \boldsymbol{n})^2) = -\kappa^2(\boldsymbol{d}_p \cdot \boldsymbol{t})^2. \tag{3.2.2}$$

Exploiting the expression of the discretized Laplace-Beltrami operator (3.2.2), we have

$$\sqrt{1+\frac{\Delta_\Gamma}{\kappa^2}} = |\boldsymbol{d}_p \cdot \boldsymbol{n}|. \tag{3.2.3}$$

By using (3.2.3), we obtain the final form

$$\mathcal{B} = \imath\kappa|\boldsymbol{d}_p \cdot \boldsymbol{n}|. \tag{3.2.4}$$

- Padé:

recalling (1.2.6) and (1.2.7), we have

$$\begin{aligned}\partial_{\boldsymbol{n}_i} u_i^P = \mathcal{R}u_i^P &= \imath\kappa e^{\imath\phi/2}\left[1+\frac{2}{M}\sum_{n=1}^{N} c_n\left(1-\frac{e^{\imath\phi}(c_n+1)}{(e^{\imath\phi}c_n+1)+\Delta_\Gamma/\kappa^2}\right)\right] u_i^P \\ &= \imath\kappa e^{\imath\phi/2}\left(\sum_{p=1}^{P}\alpha_{T_i,p}v_p + \frac{2}{M}\sum_{n=1}^{N} c_n\left(\sum_{p=1}^{P}\alpha_{T_i,p}v_p - \tilde{u}\right)\right),\end{aligned}$$

where $\tilde{u}$ is such that

$$(e^{\imath\phi}c_n + 1 + \Delta_\Gamma/\kappa^2)\tilde{u} = e^{\imath\phi}(c_n+1)\sum_{p=1}^{P}\alpha_{T_i,p}v_p. \tag{3.2.5}$$

Let us observe that

$$\Delta_\Gamma = \Delta - \partial_{\boldsymbol{nn}} = \partial_{\boldsymbol{xx}} + \partial_{\boldsymbol{yy}} - \partial_{\boldsymbol{nn}},$$

and that

$$\begin{aligned}\Delta_\Gamma u_i^P = \Delta_\Gamma\sum_{p=1}^{P}\alpha_{T_i,p}v_p &= \sum_{p=1}^{P}\alpha_{T_i,p}(\partial_{\boldsymbol{xx}}+\partial_{\boldsymbol{yy}}-\partial_{\boldsymbol{nn}})v_p \\ &= \sum_{p=1}^{P}\alpha_{T_i,p}((\boldsymbol{d}_p\cdot\boldsymbol{e}_1)^2+(\boldsymbol{d}_p\cdot\boldsymbol{e}_2)^2-(\boldsymbol{d}_p\cdot\boldsymbol{n})^2)(-\kappa^2)v_p \\ &= -\kappa^2\sum_{p=1}^{P}\alpha_{T_i,p}((\boldsymbol{d}_p^1)^2+(\boldsymbol{d}_p^2)^2-(\boldsymbol{d}_p\cdot\boldsymbol{n})^2)v_p \\ &= -\kappa^2\sum_{p=1}^{P}\alpha_{T_i,p}(1-(\boldsymbol{d}_p\cdot\boldsymbol{n})^2)v_p.\end{aligned}$$

Given the differential equation (3.2.5), $\tilde{u}$ must have the form $\tilde{u} = \sum_{p=1}^{P} \tilde{u}_p \alpha_{T_i,p} v_p$, so we have

$$\sum_{p=1}^{P} \left(e^{\imath\phi} c_n + (\boldsymbol{d}_p \cdot \boldsymbol{n})^2 \right) \tilde{u}_p \alpha_{T_i,p} v_p = \sum_{p=1}^{P} e^{\imath\phi}(c_n + 1) \alpha_{T_i,p} v_p,$$

$$\tilde{u}_p = \frac{e^{\imath\phi}(c_n + 1)}{e^{\imath\phi} c_n + (\boldsymbol{d}_p \cdot \boldsymbol{n})^2},$$

therefore

$$\mathcal{R} = \imath\kappa e^{\imath\phi/2} \left(1 + \frac{2}{M} \sum_{n=1}^{N} c_n \frac{(\boldsymbol{d}_p \cdot \boldsymbol{n})^2 - e^{\imath\phi}}{e^{\imath\phi} c_n + (\boldsymbol{d}_p \cdot \boldsymbol{n})^2} \right). \tag{3.2.6}$$

Let us conclude by recalling that, in the case of regular curved boundaries, in Section 1.2.3, we saw an improved ABC (1.2.8) thanks to the addition of the operator $\mathcal{S}$ in (1.2.9). Assuming that the term $\gamma/2\kappa^2$ does not depend on $\boldsymbol{t}$ on any point of the boundary $\partial\Omega$ (for example in the case of a circle with radius R, where $\gamma = 1/R$), we have

$$\mathcal{S} = -\frac{\gamma}{2} + \frac{\gamma^2}{8(\gamma - \imath\kappa)} + \frac{\gamma}{2} (\boldsymbol{d}_p \cdot \boldsymbol{t}_i)^2. \tag{3.2.7}$$

3.3. Algebraic formulation

Formulation (2.3.1) is associated to the following algebraic linear system

$$(M - E)\alpha = c. \tag{3.3.1}$$

In order to give an explicit form to the matrices M, E and the vector c, we consider their blocks related to an element T_i and summing on all the elements we get the final result. We take into account each integral that appears in (2.3.1) and rewrite it in terms of plane wave discretization thanks to (3.1.1). The test function can be any function that belongs to the finite space generated by the plane-wave basis. So, by linearity, we can just select the elements of the basis itself, that we denote by v_q, with $q = 1, ..., P$.

Each outgoing $\mathcal{O}_i u_i$ and incoming trace $\mathcal{I}_i u_i$ is approximated by

$$\mathcal{O}_i u_i^P = \sum_{p=1}^{P} \alpha_{T_i,\boldsymbol{d}_p} \frac{1}{2} \left(\frac{1}{\imath\kappa} \partial_{\boldsymbol{n}_i} v_{\boldsymbol{d}_p} + v_{\boldsymbol{d}_p} \right),$$

$$\mathcal{I}_i u_i^P = \sum_{p=1}^{P} \alpha_{T_i,\boldsymbol{d}_p} \frac{1}{2} \left(-\frac{1}{\imath\kappa} \partial_{\boldsymbol{n}_i} v_{\boldsymbol{d}_p} + v_{\boldsymbol{d}_p} \right).$$

The previous expressions can be written in matrix form as

$$\mathcal{O}_i u_i^P = \begin{bmatrix} \Lambda^+_{T_i,\boldsymbol{d}_1} v_{\boldsymbol{d}_1} & \dots & \Lambda^+_{T_i,\boldsymbol{d}_P} v_{\boldsymbol{d}_P} \end{bmatrix} \begin{bmatrix} \alpha_{T_i,\boldsymbol{d}_1} \\ \vdots \\ \alpha_{T_i,\boldsymbol{d}_P} \end{bmatrix},$$

$$\mathcal{I}_i u_i^P = \begin{bmatrix} \Lambda^-_{T_i,\boldsymbol{d}_1} v_{\boldsymbol{d}_1} & \dots & \Lambda^-_{T_i,\boldsymbol{d}_P} v_{\boldsymbol{d}_P} \end{bmatrix} \begin{bmatrix} \alpha_{T_i,\boldsymbol{d}_1} \\ \vdots \\ \alpha_{T_i,\boldsymbol{d}_P} \end{bmatrix},$$

$$\Lambda^{\pm}_{T_i,\boldsymbol{d}_p} \coloneqq \frac{1}{2}(1 \pm \boldsymbol{d}_p \cdot \boldsymbol{n}_i).$$

From now on, for the sake of simplicity of notation, we no longer write $\boldsymbol{d}_p$, but simply p.

Let us recall that we need to take into account the boundary condition prescribed on Γ_{int}. In (1.1.2), it consisted in a Neumann boundary condition, hence we develop the computation for this case. Its extension to Dirichlet or Robin boundary condition is straightforward.

Proposition 3.1 (Algebraic formulation):
The matrices M, $E = E_1 + E_2 + E_3$ and the vector c of the linear system (3.3.1) associated to the plane wave discretization of (2.3.1) in the case of scattering problem read as

$$
\begin{aligned}
M_{ii,pq} &= \Lambda^+_{T_i,q}\Lambda^+_{T_i,p}\int_{\partial T_i} v_p\overline{v_q}ds, \\
E_{1,ij,pq} &= \Lambda^-_{T_i,q}\Lambda^+_{T_j,p}\int_{F_{ij}} v_p\overline{v_q}ds, \\
E_{2,ii,pq} &= -\frac{1}{2}\Lambda^-_{T_i,q}\int_{\Gamma_i^{\text{ext}}} v_p\overline{v_q}ds, && \imath\kappa \\
E_{2,ii,pq} &= -\frac{1}{2}\Lambda^-_{T_i,q}|\boldsymbol{d}_p\cdot\boldsymbol{n}|\int_{\Gamma_i^{\text{ext}}} v_p\overline{v}_q ds, && \text{sqrt} \\
E_{2,ii,pq} &= -\frac{e^{\imath\phi/2}}{2}\Lambda^-_{T_i,q}\left(1+\frac{2}{M}\sum_{n=1}^{N} c_n\frac{(\boldsymbol{d}_p\cdot\boldsymbol{n})^2-e^{\imath\phi}}{e^{\imath\phi}c_n+(\boldsymbol{d}_p\cdot\boldsymbol{n})^2}\right)\int_{\Gamma_i^{\text{ext}}} v_p\overline{v}_q ds, && \text{Padé} \\
\tilde{E}_{2,ii,pq} &= -\frac{1}{2\imath\kappa}\Lambda^-_{T_i,q}\left(-\frac{\gamma}{2}+\frac{\gamma^2}{8(\gamma-\imath\kappa)}+\frac{\gamma}{2}(\boldsymbol{d}_p\cdot\boldsymbol{t}_i)^2\right)\int_{\Gamma_i^{\text{ext}}} v_p\overline{v_q}ds, && (*) \\
E_{3,ii,pq} &= \frac{1}{2}\Lambda^-_{T_i,q}\int_{\Gamma_i} v_p\overline{v_q}ds, \\
c_{i,q} &= -\frac{1}{2\imath\kappa}\Lambda^-_{T_i,q}\int_{\Gamma_i^{\text{int}}} g\overline{v_q}ds,
\end{aligned}
$$

where the indexes $i, j = 1, ..., K$ identify the block related to the boundary of an element T_i or the face shared by two elements T_i, T_j and the indexes $p, q = 1, ..., P$ identify one of its elements. The additional term $(*)$ refers to the case of improved ABC for curved boundaries.

Proof.

Matrix M: Let us start with the first integral that appears in (2.3.1) whose manipulation will consist in the matrix M.

$$
\int_{\partial T_i}\frac{1}{2}\left(\frac{1}{\imath\kappa}\frac{\partial u_i^P}{\partial \boldsymbol{n}_i}+u_i^P\right)\overline{\frac{1}{2}\left(\frac{1}{\imath\kappa}\frac{\partial v_q}{\partial \boldsymbol{n}_i}+v_q\right)} = \Lambda^+_{T_i,q}\sum_{p=1}^{P}\Lambda^+_{T_i,p}\alpha_{T_i,p}\int_{\partial T_i} v_p\overline{v_q}ds = M_{ii}\alpha_{T_i,q}
$$

Since M is a block-diagonal matrix, we can use three indexes i, p, q instead of four to represent each of its elements as

$$
M_{ii,pq} = \Lambda^+_{T_i,q}\Lambda^+_{T_i,p}\int_{\partial T_i} v_p\overline{v_q}ds.
$$

Matrix E_1: Let us proceed with the third integral whose approximation will appear as a part of matrix E, that we denote by E_1

$$\int_{F_{ij}} \frac{1}{2}\left(\frac{1}{\imath\kappa}\frac{\partial u_j^P}{\partial \boldsymbol{n}_j} + u_j^P\right)\overline{\frac{1}{2}\left(-\frac{1}{\imath\kappa}\frac{\partial v_q}{\partial \boldsymbol{n}_i} + v_q\right)} = \Lambda^-_{T_i,q}\sum_{p=1}^{P}\Lambda^+_{T_j,p}\alpha_{T_j,p}\int_{F_{ij}} v_p\overline{v_q}ds = E_{1,ij}\alpha_{T_j,q}.$$

Since E_1 is not a block-diagonal matrix, we need to use all four indexes i, j, p, q to represent each of its elements as

$$E_{1,ij,pq} = \Lambda^-_{T_i,q}\Lambda^+_{T_j,p}\int_{F_{ij}} v_p\overline{v_q}ds.$$

Matrix E_2: In order to deal with the second integral that will be a part of the matrix E and that we denote by E_2, we need to handle the expression of the Absorbing Boundary Condition in terms of: zeroth-order approximation ($\imath\kappa$), exact computation (sqrt) and high-order approximation (Padé).

- $\imath\kappa$:

The plane-wave discretization of the zeroth-order ABC is straightforward recalling (3.2.1)

$$\int_{\Gamma_i^{\text{ext}}} \frac{1}{2}\left(-\frac{1}{\imath\kappa}\imath\kappa u_i^P\right)\overline{\frac{1}{2}\left(-\frac{1}{\imath\kappa}\frac{\partial v_q}{\partial \boldsymbol{n}} + v_q\right)} = -\frac{1}{2}\Lambda^-_{T_i,q}\sum_{p=1}^{P}\alpha_{T_i,p}\int_{\Gamma_i^{\text{ext}}} v_p\overline{v_q}ds = E_{2,ii,pq}\alpha_{T_i,q}.$$

Thus, each element of the block-diagonal matrix E_2 can be expressed as

$$E_{2,ii,pq} = -\frac{1}{2}\Lambda^-_{T_i,q}\int_{\Gamma_i^{\text{ext}}} v_p\overline{v_q}ds.$$

- sqrt:

By using (3.2.4), we end up with

$$\int_{\Gamma_i^{\text{ext}}} \frac{1}{2}\left(-\frac{1}{\imath\kappa}\mathcal{B}u_i^P\right)\overline{\frac{1}{2}\left(-\frac{1}{\imath\kappa}\frac{\partial v_q}{\partial \boldsymbol{n}} + v_q\right)} = -\frac{1}{2}\Lambda^-_{T_i,q}\sum_{p=1}^{P}|\boldsymbol{d}_p\cdot\boldsymbol{n}|\alpha_{T_i,p}\int_{\Gamma_i^{\text{ext}}} v_p\overline{v}_q ds = E_{2,ii,pq}\alpha_{T_i,q}.$$

So that each element of E_2 can be written as

$$E_{2,ii,pq} = -\frac{1}{2}\Lambda^-_{T_i,q}|\boldsymbol{d}_p\cdot\boldsymbol{n}|\int_{\Gamma_i^{\text{ext}}} v_p\overline{v}_q ds.$$

- Padé:

Substituting (3.2.6) in the second term of (2.3.1), where - in the framework of approximation - the operator $\mathcal{R}$ approximates the operator $\mathcal{B}$, as we have seen in Section 1.2.3, we have

$$\int_{\Gamma_i^{\text{ext}}} \frac{1}{2}\left(-\frac{1}{\imath\kappa}\mathcal{R}u_i^P\right)\overline{\frac{1}{2}\left(-\frac{1}{\imath\kappa}\frac{\partial v_q}{\partial \boldsymbol{n}}+v_q\right)}$$

$$= -\frac{e^{\imath\phi/2}}{2}\Lambda^-_{T_i,q}\sum_{p=1}^{P}\left(1+\frac{2}{M}\sum_{n=1}^{N}c_n\frac{(\boldsymbol{d}_p\cdot\boldsymbol{n})^2-e^{\imath\phi}}{e^{\imath\phi}c_n+(\boldsymbol{d}_p\cdot\boldsymbol{n})^2}\right)\alpha_{T_i,p}\int_{\Gamma_i^{\text{ext}}} v_p\overline{v}_q ds = E_{2,ii}\alpha_{T_i,q}.$$

Thus, eventually we have

$$E_{2,ii,pq} = -\frac{e^{\imath\phi/2}}{2}\Lambda^-_{T_i,q}\left(1+\frac{2}{M}\sum_{n=1}^{N}c_n\frac{(\boldsymbol{d}_p\cdot\boldsymbol{n})^2-e^{\imath\phi}}{e^{\imath\phi}c_n+(\boldsymbol{d}_p\cdot\boldsymbol{n})^2}\right)\int_{\Gamma_i^{\text{ext}}} v_p\overline{v}_q ds.$$

In the case of regular curved boundary, recalling (3.2.7), the additional term gains the discretized form

$$\int_{\Gamma_i^{\text{ext}}} \frac{1}{2}\left(-\frac{1}{\imath\kappa}\mathcal{S}u_i^p\right)\overline{\frac{1}{2}\left(-\frac{1}{\imath\kappa}\frac{\partial v_q}{\partial \boldsymbol{n}_i}+v_q\right)}$$

$$= -\frac{1}{2\imath\kappa}\Lambda^-_{T_i,q}\sum_{p=1}^{P}\left(-\frac{\gamma}{2}+\frac{\gamma^2}{8(\gamma-\imath\kappa)}+\frac{\gamma}{2}(\boldsymbol{d}_p\cdot\boldsymbol{t}_i)^2\right)\alpha_{T_i,p}\int_{\Gamma_i^{\text{ext}}} v_p\overline{v_q} ds,$$

that can be written as a part of E_2 with the additional term

$$\tilde{E}_{2,ii,pq} = -\frac{1}{2\imath\kappa}\Lambda^-_{T_i,q}\left(-\frac{\gamma}{2}+\frac{\gamma^2}{8(\gamma-\imath\kappa)}+\frac{\gamma}{2}(\boldsymbol{d}_p\cdot\boldsymbol{t}_i)^2\right)\int_{\Gamma_i^{\text{ext}}} v_p\overline{v_q} ds.$$

Matrix E_3: Matrix E_3, that is the last part that completes matrix E, consists in the following plane wave discretization of the fourth integral

$$\int_{\Gamma_i}\frac{1}{2}u_i^P\overline{\frac{1}{2}\left(-\frac{1}{\imath\kappa}\frac{\partial v_q}{\partial \boldsymbol{n}_i}+v_q\right)} = \frac{1}{2}\Lambda^-_{T_i,q}\sum_{p=1}^{P}\alpha_{T_i,p}\int_{\Gamma_i} v_p\overline{v_q} ds = E_{3,ii}\alpha_{T_i,q}.$$

Hence, each element of the block-diagonal matrix E_3 reads

$$E_{3,ii,pq} = \frac{1}{2}\Lambda^-_{T_i,q}\int_{\Gamma_i} v_p\overline{v_q} ds.$$

Vector c: Finally, vector c consists in the following plane wave discretization of the r.h.s of (2.3.1)

$$\int_{\Gamma_i^{\text{int}}} -\frac{1}{2\imath\kappa} g \overline{\frac{1}{2}\left(-\frac{1}{\imath\kappa}\frac{\partial v_q}{\partial \boldsymbol{n}_i} + v_q\right)} = -\frac{1}{2\imath\kappa}\Lambda^-_{T_i,q}\int_{\Gamma_i^{\text{int}}} g\overline{v}_q ds = c_{T_i,q},$$

that corresponds to its index form

$$c_{i,q} = -\frac{1}{2\imath\kappa}\Lambda^-_{T_i,q}\int_{\Gamma_i^{\text{int}}} g\overline{v_q} ds.$$

□

Let us observe again that M is a block-diagonal matrix, whose diagonal blocks are the matrices M_{T_i} related to the elements $T_i \in \mathcal{T}$. Conversely, although E_2 and E_3 are block-diagonal matrices, E can not be block-diagonal, since E_1 is not one, because of the presence of non-null blocks related to adjacent elements to each T_i.

Let us remark that the matrices M and E have dimension (PK, PK) and the vector c has dimension PK, where P is the number of basis functions and K the number of elements of the mesh.

3.4. Theoretical and computational aspects

3.4.1. Convergence

In this section, we limit to present a quick overview of convergence results regarding classical refinements known in the literature.

Both h-refinement ([38]), that is mesh subdivision, p-refinement ([39]), that is local basis enrichment, and hp-refinement ([40, 41]), that is the combination of the previous two, are suitable and appropriate for the method. Once an element of the mesh is selected for a refinement, the type of the refinement needs to be decided. This choice depends on the nature of the solution: if it is smooth, a p-refinement will be more efficient at reducing the error, if that is not the case, an h-refinement should be preferred. Nevertheless, clearly, the previous considerations are relevant only when the exact solution is known *a priori*, while, if it is not unknown, *a posteriori* error estimators do not indicate the type of refinement which should be undertaken, but some algorithms have been tested in the literature ([42]).

In [43] a very detailed and complete analysis concerning the plane-wave approximation of homogeneous Helmholtz solutions complemented by proofs is provided. Because of the technical difficulty and the extension of the study, we limit ourselves to briefly retrace the main steps and introduce the key features.

The setting is the one of the homogeneous Helmholtz equation in $\mathbb{R}^n$. We take $n = 2$, nevertheless explicit estimates were derived for either $n = 2$ and $n = 3$ in the paper. We consider the approximation space of plane-waves

$$PV_{\kappa,P}(\mathbb{R}^2) = \{v \in \mathbb{C}^\infty(\mathbb{R}^2) : v(\boldsymbol{x}) = \sum_{p=1}^{P} \alpha_p e^{\imath\kappa \boldsymbol{d}_p \cdot \boldsymbol{x}}, \alpha_p \in \mathbb{C}\}, P \in \mathbb{N},$$

and the space of the so-called generalized harmonic polynomials

$$HP_{\kappa,L}(\mathbb{R}^2) = \{w \in \mathbb{C}^\infty(\mathbb{R}^2) : w(\boldsymbol{x}) = \sum_{l=-L}^{L} \beta_l e^{\imath l\psi} J_{|l|}(\kappa r), \beta_l \in \mathbb{C}\}, L \in \mathbb{N},$$

where (r, ψ) denotes polar coordinates and J_l the Bessel function of the first kind.

The idea is to proceed by steps: the first one is to provide an approximation of Helmholtz solutions by generalized harmonic polynomials, the second one to retrieve an approximation of the latters by plane waves and, eventually, combine the results concerning the previous two steps to gain an approximation of Helmholtz solutions by plane waves.

In the first intermediate step, Vekua's theory ([44]) is crucial. It provides the so-called Vekua operators, namely integral operators that map harmonic functions to solutions of the homogeneous Helmholtz equation and vice versa. In particular, they take harmonic polynomials to generalized harmonic polynomials. Their continuity lets approximation estimates for the homogeneous Helmholtz solutions in $HP_{\kappa,L}(\mathbb{R}^2)$ starting from approximation estimates of harmonic functions by harmonic polynomials.

In the second step, generalized harmonic polynomials are approximated by a finite linear combination of circular waves. The Jacobi-Anger expansion of the element $\sum_{p=1}^{P} \alpha_p e^{\imath\kappa \boldsymbol{d}_p \cdot \boldsymbol{x}}$ of $PV_{\kappa,P}(\mathbb{R}^2)$ is truncated and the resulting linear system with the unknowns α_p is to be solved. Eventually, error bounds are obtained by estimating the residual error related to the truncation of the Jacobi-Anger expansion.

In the third and final step, Sobolev norms need to be linked to the L^∞-norm in order to exploit the estimates provided in the first two steps which are given in terms of the L^∞-norm. The latter operation leads to an *hp*-estimate.

3.4.2. Ill-conditioning

The linear system obtained by plane-wave discretization is inclined to ill-conditioning whenever the trial space has high dimension because of a big number of elements in the mesh or of a big number of plane-waves used and this is due to an instability of the plane-waves basis ([45, 46]). Indeed, if the elements have a relatively small size compared to the wavelength, that is $|\boldsymbol{x}| \ll \kappa^{-1}$, the plane-wave functions $\boldsymbol{x} \mapsto \exp(\imath\kappa \boldsymbol{d}_p \cdot \boldsymbol{x})$ are almost constant, therefore they are nearly linearly dependent. Moreover, even in the case of elements whose size is comparable to the wavelength, plane-waves become hard to distinct whenever their density increases.

In particular, considering the block M_{T_i}, it is possible to empirically observe that its spectral conditioning number increases like $\sim h_{T_i}^{-q}$ for element size $h_{T_i} \to 0$, where q is proportional to the number P_{T_i} of plane-waves. Moreover, unfortunately, the condition number exponentially rises in q, that is $\mathrm{cond}(M_{T_i}) \sim e^{\alpha q}$ for $q \to \infty$ and $\alpha > 0$. A completely similar dramatic growth of the condition number can be observed for the full matrix as the mesh is refined or more plane-waves are exploited on each element.

Several heuristic algorithms have been tested in order to cope with the ill-conditioning. For example, limiting P_{T_i} by monitoring the condition numbers of element matrices seems also to lead to a curbing of the condition number of the full matrix ([47]). Other techniques *a priori* prescribe the number of plane-waves P_{T_i}, such as the estimate $P_{T_i} = \mathrm{round}(\kappa h_{T_i} + C(\kappa h_{T_i})^{1/3})$ with $3 \leq C \leq 14$ ([48]). A method based on the local orthogonalization of the plane-wave basis turned out to be effective in lowering the condition number of the global system matrix ([49]). Lastly, some preconditioning methods based on local preconditioners have been studied ([36, 46]) and they are equivalent to an orthonormalisation of the plane-waves basis with respect to an L^2 inner product computed on the boundary of the elements.

We highlight the fact that ill-conditioning is one of the main problems that the Trefftz method in the framework of Helmholtz presents, which may make any kind of refinement hard to pursue. Therefore, it is important to keep trace of it in order to avoid unreliable results. In the last chapter, which is the one devoted to the numerical experiments, the conditioning is always kept into account to interpret the results and understand the best method which can be applied to achieve better results.

3.4.3. Adaptivity

Besides the h and p refinements, which are common to all finite element methods, directional adaptivity finds application in our framework. The key aspect is that, in the simple case in which the exact solution is a plane wave, if the direction of one of the plane wave basis functions is aligned with the one of the exact solution, the method exactly recovers the analytical solution, up to rounding errors. Thus, the key idea is to rotate the basis associated to an element according to its dominant direction, which clearly needs to be numerically estimated *a posteriori*. An algorithm based on the study of the properties of the Hessian and its principal eigenvector of the numerical solution is presented in ([40]). It is important to observe that directional adaptivity permits good results only in the case of rather simple geometries, that is when there is only one dominant wave direction. Nevertheless, complex geometries may lead to multiple dominant wave directions which are way harder to tackle by bare directional adaptivity.

As we said in the previous section, ill-conditioning is a very serious issue, therefore any kind of refinement needs to be carefully taken into consideration. Of course, the best option would be to apply a refinement only to critical areas, which are those characterized by rather complex geometries or by special importance, in order to exploit the refinement only on the areas that require it.

4 | Preliminary numerical study

In this chapter, we study the UWVF with ABC in the simplest setting, that is a computational domain composed of a single mesh cell. In a progressive approach, several configurations are taken into account, in particular we consider different approximations of the ABC to study their behaviour and various sets of basis to explore the features of directional adaptivity.

4.1. One-element benchmark

Let $\Omega = (0,1) \times (0,1)$ be a domain. We consider the following model boundary-value problem set in terms of Helmholtz equation for $u : \Omega \to \mathbb{C}$

$$\begin{cases} \Delta u + \kappa^2 u = 0, & \boldsymbol{x} \in \Omega, \\ \partial_{\boldsymbol{n}} u = \mathcal{B} u, & \boldsymbol{x} \in \Gamma^{\mathrm{ABC}}, \\ \partial_{\boldsymbol{n}} u = g, & \boldsymbol{x} \in \Gamma^{\mathrm{N}}, \end{cases} \tag{4.1.1}$$

where Γ^{ABC} stands for the portion of boundary of Ω on which Absorbing Boundary Conditions are applied , Γ^N for its complementary on which Neumann boundary conditions are applied, so that $\partial\Omega = \Gamma^{ABC} \cup \Gamma^N$, as usual $\boldsymbol{n}$ is the outward unit normal on the boundary of Ω and $\mathcal{B}$ is a suitable trace operator that permits to model absorption on Γ^{ABC} defined as (1.2.4). Lastly, in (4.1.1) we wrote a Neumann boundary condition on Γ^N with a given function g, that can be easily retrieved exploiting the exact solution $u^{\mathrm{ref}}(\boldsymbol{x}) = e^{\imath\kappa(\widehat{\boldsymbol{d}}\cdot\boldsymbol{x})}$, $\widehat{\boldsymbol{d}} = (\cos\alpha, \sin\alpha)^T, \alpha \in [0, 2\pi]$.

We take as reference configuration the one which prescribes exact Neumann boundary conditions on the whole boundary $\partial\Omega$, that is $\Gamma^{ABC} = \varnothing$ and we denote 'Neumann'.

Moreover, we consider 2 settings:

1. $\Gamma^{ABC} = \{(x, y) \in \mathbb{R}^2 : x = 1, y \in (0, 1)\}$, that we denote by the number 1 (ABCs are applied on 1 edge);
2. $\Gamma^{ABC} = \{(x, y) \in \mathbb{R}^2 : x = 1, y \in (0, 1)\} \cup \{(x, y) \in \mathbb{R}^2 : x \in (0, 1), y = 1\}$, that we denote by the number 2 (ABCs are applied on 2 edges).

In the previous 2 settings, the operator $\mathcal{B}$ is treated in 3 different ways:

1. Approximation of $\mathcal{B} = \imath\kappa$, that we denote '$\imath\kappa$'.
2. Exact computation of $\mathcal{B}$, that we denote 'sqrt'.
3. Approximation of $\mathcal{B} = \mathcal{R}$, where $\mathcal{R}$ is the approximate form of $\mathcal{B}$ by Padé approximation of the square root, that we denote 'Padé'.

We begin by focusing on the study of the numerical properties of the basis. Indeed, the simplicity of the benchmark lets us investigate the possibility of directional adaptivity. In particular, we consider three sets of shape functions:

- "full" basis: it is composed by P plane-waves whose directions are uniformly spaced in the whole plane, that is $\boldsymbol{d}_p = (\cos\theta_p, \sin\theta_p)^T$, $0 \leq \theta_p \leq 2\pi, p = 1, ..., P$;
- "half" basis: it is composed by P plane-waves whose directions are uniformly spaced in a half plane in a symmetric way with respect to $\hat{\alpha}$ which is a reference angle, that is $\boldsymbol{d}_p = (\cos\theta_p, \sin\theta_p)^T$, $\hat{\alpha} - \pi/2 \leq \theta_p \leq \hat{\alpha} + \pi/2, p = 1, ..., P$;
- "quarter" basis: it is composed by P plane-waves whose directions are uniformly spaced in a quarter plane in a symmetric way with respect to $\hat{\alpha}$ which is a reference angle, that is $\boldsymbol{d}_p = (\cos\theta_p, \sin\theta_p)^T$, $\hat{\alpha} - \pi/4 \leq \theta_p \leq \hat{\alpha} + \pi/4, p = 1, ..., P$.

4.2. Study of the projection error

We want to compute the projection of a given plane-wave $u^{\text{ref}}(\boldsymbol{x}) = e^{\imath\kappa\hat{\boldsymbol{d}}\cdot\boldsymbol{x}}$, $\hat{\boldsymbol{d}} = (\cos\alpha, \sin\alpha)^T$ onto the approximation space, that is the one generated by the basis $\{\phi_p(\boldsymbol{x}) = e^{\imath\kappa\boldsymbol{d}_p\cdot\boldsymbol{x}}\}_{p=1,...,P}$. In order to do so, we need to compute the coefficients $\{\alpha_p\}_{p=1,...,P}$ by solving the following linear system (normal equation)

$$\sum_{p=1}^{P} \alpha_p \int_\Omega \phi_p \overline{\phi}_q d\boldsymbol{x} = \int_\Omega u^{\text{ref}} \overline{\phi}_q d\boldsymbol{x}, \qquad q = 1, ..., P.$$

Once the coefficients $\{\alpha_p\}_{p=1,...,P}$ of the projected function $\hat{u} = \sum_{p=1}^{P} \alpha_p \phi_p$ are determined, we compute the relative L^2-error, that is

$$\hat{\epsilon} = \frac{||u^{\text{ref}} - \hat{u}||_{L^2(\Omega)}}{||u^{\text{ref}}||_{L^2(\Omega)}},$$

which corresponds to the best approximation error.

The relative L^2-error is plotted as a function of the angle α in Fig. 4.1. For the "full" basis, we let α vary in $[0; 2\pi]$, while for the "half" and "quarter" basis cases we fix $\hat{\alpha} = 0$ and we let α vary respectively in $[-\pi/2; \pi/2]$ and $[-\pi/4; \pi/4]$.

As expected, observing Fig. 4.1, we can see that the error is null whenever the reference solution is aligned with one of the shape functions. From the results reported in Fig. 4.1.a, we can claim that the error is maximum when the misalignment is maximum, that is when the reference solution is between two consecutive shape functions. Moreover, considering Fig. 4.1.b and Fig. 4.1.c, we can state a similar behaviour, but also a smaller error whenever the reference solution is in the middle area spaced by the set of shape functions. Lastly, the smaller is the portion of plane covered by the basis, the smaller is the error.

We can guess that a "half" and "quarter" basis lead to a smaller error when they are exploited to approximate a plane-wave, provided that the plane-wave that is approximated is contained respectively into the half plane and quarter plane covered by the basis themselves. The previous hypothesis is satisfied by those portions of the boundary $\partial\Omega$ on which an ABC is prescribed by taking as half or quarter plane the one that corresponds to the outer half or quarter plane with respect to the domain Ω.

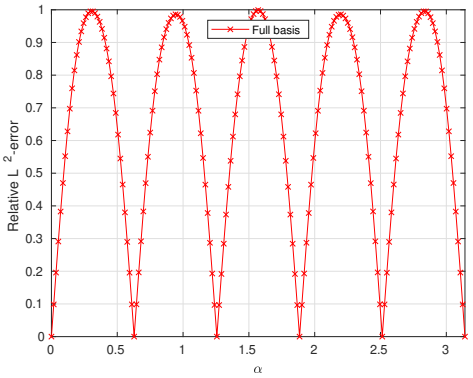

(a) "Full" basis: $P = 10, \Delta\theta = \pi/5$

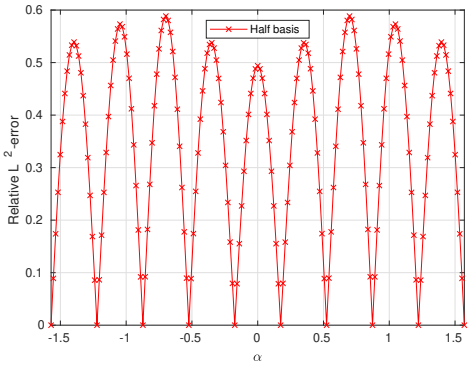

(b) "Half" basis: $P = 10, \Delta\theta = \pi/9$

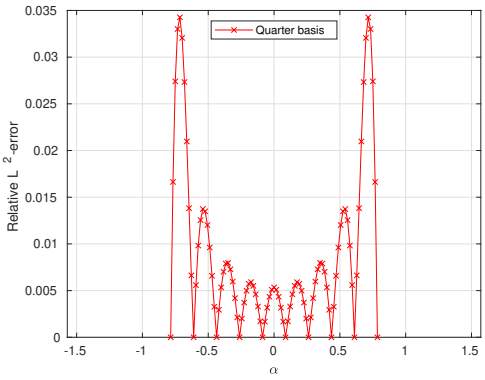

(c) "Quarter" basis: $P = 10, \Delta\theta = \pi/18$

Figure 4.1: Propagative wave benchmark with square domain: best approximation L^2-error w.r.t. α with $P = 10$.

Notice that these results are valid when P is fixed and so, reducing the portion of plane covered by the basis, we end up with a smaller angle between the shape functions. Now we want to check the behaviour of the three sets of basis once the angle between the shape functions is fixed, that is we end up with less shape functions reducing the portion of plane covered by the basis. Indeed, the conditioning of the matrix of the linear system (3.3.1) is mainly due to P, hence we aim at using the fewest shape functions as possible.

We fix the angle between all the shape functions as $\Delta\theta = \pi/18$, therefore we end up with $P = 36, P = 18$ and $P = 10$ respectively for "full", "half" and "quarter" basis. Unfortunately, observing Fig. 4.2, we can see that the bare removal of the shape functions that are not contained in the portion of plane covered by the basis is not enough to lead to a smaller error.

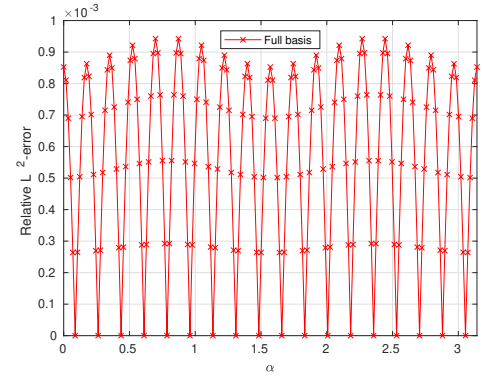

(a) "Full" basis: $P = 36, \Delta\theta = \pi/18$

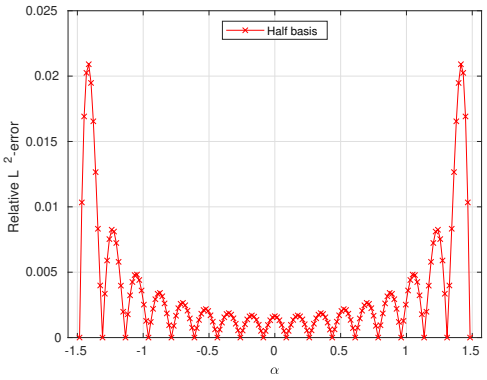

(b) "Half" basis: $P = 18, \Delta\theta = \pi/18$

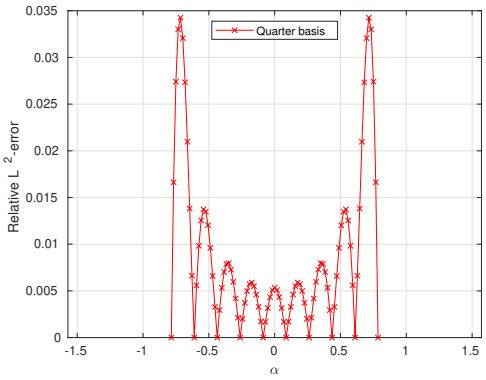

(c) "Quarter" basis: $P = 10, \Delta\theta = \pi/18$

Figure 4.2: Propagative wave benchmark with square domain: best approximation L^2-error w.r.t. α with $\Delta\theta = \pi/18$.

The conclusion is that the key aspect is embodied by the density of the shape functions, that is - provided a good conditioning of the matrix of the linear system (3.3.1) - the denser are the basis, the smaller is the error. For a given P, it is better to reduce the range of α, that is equivalent to take plane-waves basis functions whose direction is close to the one of the reference solution. For a given $\Delta\theta$, plane-waves whose orientation is far from the one of the reference solution still contribute to improve the accuracy of the numerical solution.

Hence, what it is possible to do is recognizing those portion of the boundary $\partial\Omega$ on which an ABC is prescribed and accordingly choose a set of shape functions which cover the smallest portion of the plane as possible. Indeed, the prescription of an ABC is equivalent to an *a priori* knowledge of the local direction of the exact solution: it is outgoing, therefore it crosses that portion of the boundary $\partial\Omega$ with an angle that depends on its local geometry.

Considering our test cases: in "case 1", that corresponds to $\Gamma^{ABC} = \{(x, y) \in \mathbb{R}^2 : x = 1, y \in (0, 1)\}$, we assume that the exact solution crosses Γ^{ABC} which is equivalent to take $-\pi/2 \leq \alpha \leq \pi/2$, while in "case 2", that corresponds to $\Gamma^{ABC} = \{(x, y) \in \mathbb{R}^2 : x = 1, y \in (0, 1)\} \cup \{(x, y) \in \mathbb{R}^2 : x \in (0, 1), y = 1\}$, it is equivalent to take $0 \leq \alpha \leq \pi/2$. Thus, the best choice of set of shape functions in "case 1" is a "half" basis with $\hat{\alpha} = 0$, while in "case 2" it is a "quarter" basis with $\hat{\alpha} = \pi/4$.

4.3. Study of the numerical error with the UWVF

In the second part of this section, we present the numerical results concerning the different scenarios described in Section 4.1. We pick as exact solutions plane-waves with $\alpha = 0$ and $\alpha = \pi/4$, $\kappa = 20$. The plots are shown here below in Fig. 4.3.

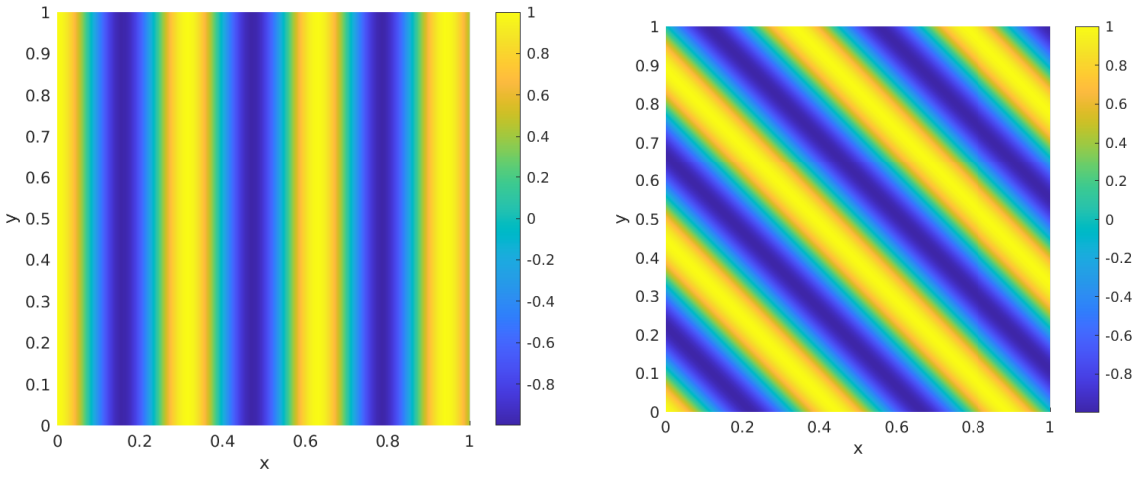

(a) $\alpha = 0$ (b) $\alpha = \pi/4$

Figure 4.3: Propagative wave benchmark with square domain: exact solution.

We exploit the Ultra Weak Variational Formulation and its plane-wave discritization as respectively presented in Chapter 2 and Chapter 3. Nevertheless, since we do not consider a mesh, the term related to the interface between two different elements is null.

We define the relative L^2-error as follows

$$\epsilon = \frac{||u^{\text{ref}} - u^P||_{L^2(\Omega)}}{||u^{\text{ref}}||_{L^2(\Omega)}}.$$

4.3.1. Results with "full" basis

We exploit a "full" basis, fix the shift $\theta_1 = \pi\frac{\sqrt{2}}{2}$ and plot the relative L^2-error with respect to P, for $P = 1, ..., 120$. The plots are shown here below in Fig. 4.4.

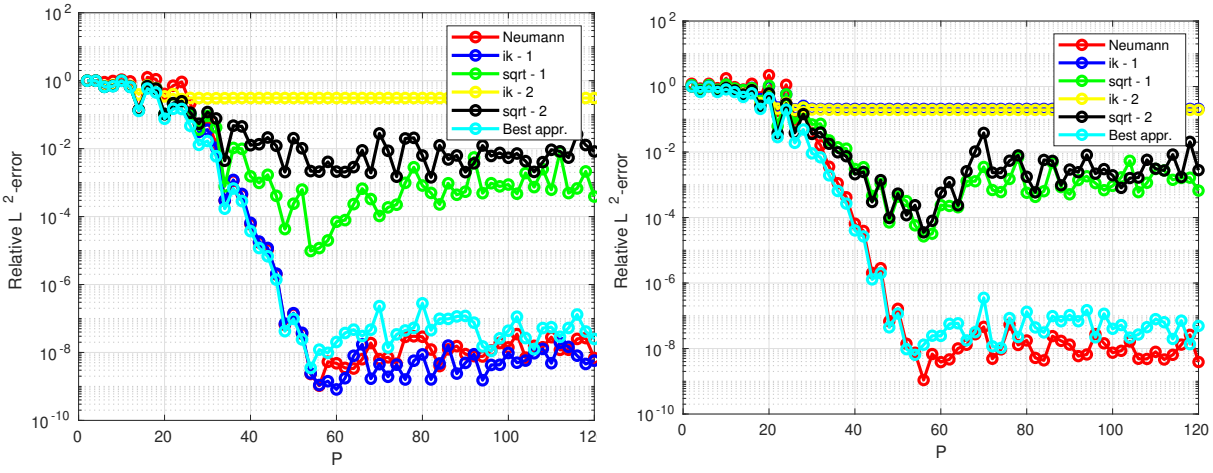

(a) $\alpha = 0$ (b) $\alpha = \pi/4$

Figure 4.4: Propagative wave benchmark with square boundary: relative L^2-error w.r.t. P with "full" basis and several B.C.

We can do the following observations:

- After a certain threshold P_{MAX} (for both cases $P_{\text{MAX}} \approx 60$) results are not accurate anymore. This is likely due to the fact that the matrix $(M - E)$ associated to the linear system (3.3.1) becomes ill-conditioned.

  Indeed, fixed the wave number κ, observing Fig. 4.5, we can claim that the conditioning strongly depends on P, while the type of ABC, the type of basis and α play no role in it: increasing P, the conditioning number $\kappa(M - E)$ becomes bigger and bigger, until a certain threshold P_{MAX} where the matrix $(M - E)$ is ill-conditioned and results are not reliable anymore, which corresponds with the very oscillating lines in the error plots.

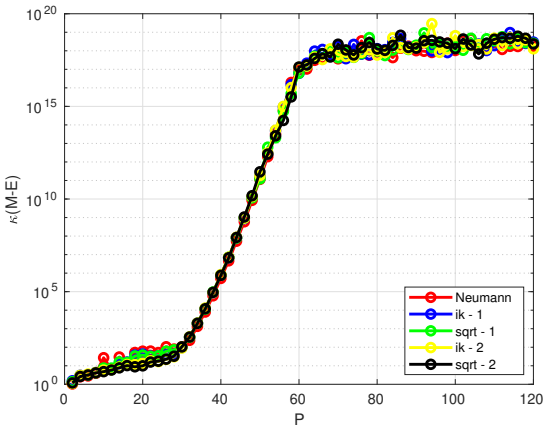

Figure 4.5: Propagative wave benchmark with square boundary: condition number w.r.t. P with $\alpha = \pi/4$, "full" basis and several B.C.

- The numerical error associated to the Neumann case is close to the best approximation one. Indeed the boundary condition is exact on the whole boundary $\partial\Omega$ and the only source of error is the numerical one associated to the plane-wave discretization.
- The $\imath\kappa$ case is the one that presents the biggest error, since it also incorporates the source of error associated to the approximate model of the ABC, nevertheless the error drops to the reference one when $\alpha = 0$ due to the fact that the approximate boundary condition turns out to be exact.
- The sqrt case has an error that is intermediate between the previous two, instead we would expect it to be close to the Neumann case since the Absorbing Boundary Condition is exact and exactly implemented, with no approximation. This result is surprising because, being the Absorbing Boundary Condition exact, we expected the numerical error to be close to the best approximation one.

4.3.2. Results with adapted basis

We can speculate that the unexpected behaviour in the sqrt case may depend on an appropriate choice of the set of basis functions. It is reasonable to use only basis functions that verify the boundary condition. Indeed, according to what we retrieved in Section 4.1.1, a basis is inappropriate whenever it contains not only all outgoing waves, but also incoming waves. To confirm this intuition, we exploit a "half" basis with $\hat{\alpha} = 0$, a "quarter" basis with $\hat{\alpha} = \pi/4$ and plot the relative L^2-error with respect to P, for $P = 1, ..., 120$, for $\alpha = \pi/4$. Notice that the "half" basis is appropriate for "case 1" (and inappropriate for "case 2" since the basis covers a portion of plane that includes also forbidden directions), while the "quarter" case is appropriate for "case 2" (and inappropriate for "case 1" since the basis covers a portion of plane that does not include admissible outgoing directions).

Observing Fig. 4.6 and comparing it with Fig. 4.4.b, we can see that picking an appropriate basis leads to a smaller error in both the sqrt cases (green and black lines).

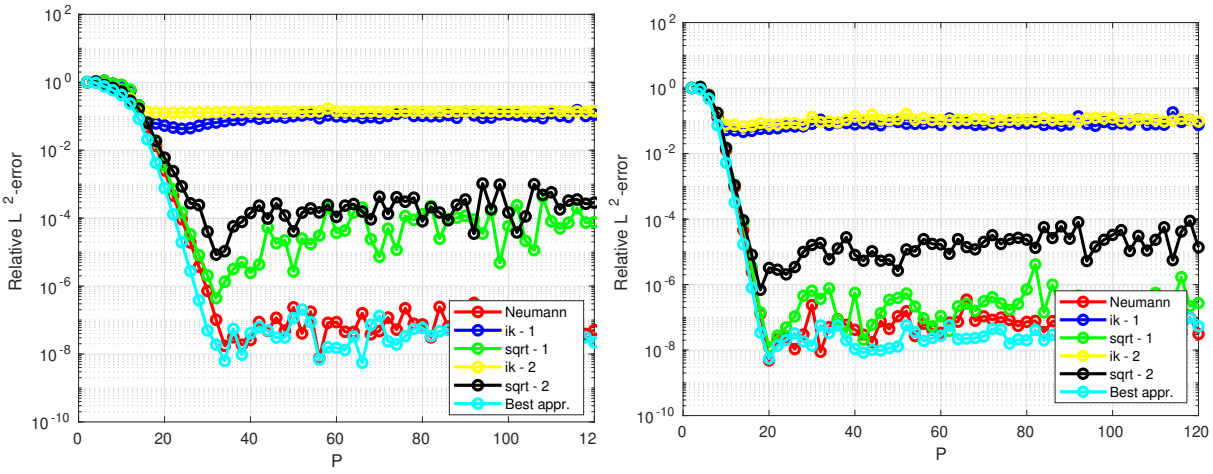

(a) "half" basis

(b) "Quarter" basis

Figure 4.6: Propagative wave benchmark with square boundary: relative L^2-error w.r.t. P with $\alpha = \pi/4$ and several B.C.

4.3.3. Results with HABC

In the third part of this section, we compare the results concerning the case $\alpha = \pi/4$, where the ABC is treated with its exact formulation (sqrt) and high-order approximation (Padé). Once again, we fix $\theta_1 = \pi\frac{\sqrt{2}}{2}$ and plot the relative L^2-error with respect to P, for $P = 1, ..., 120$.

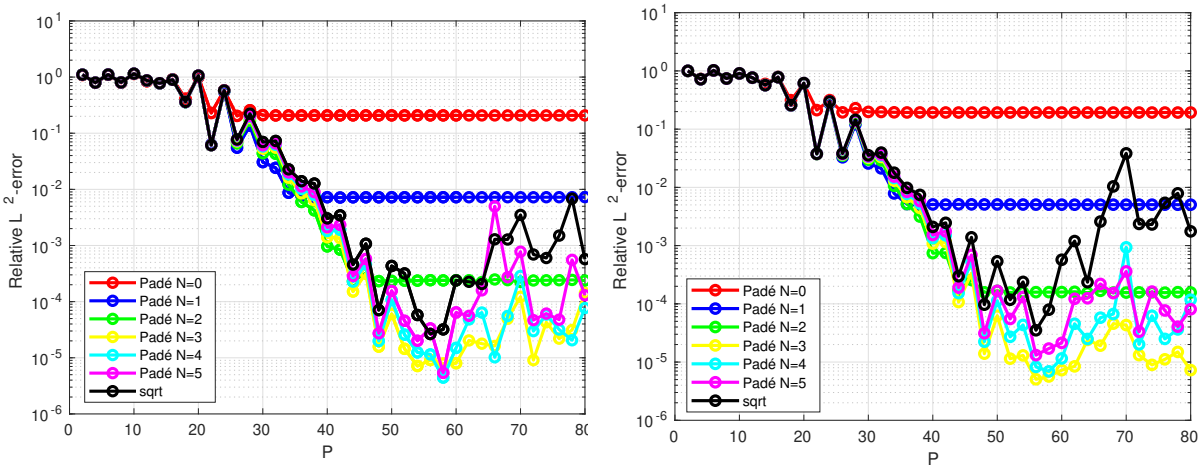

(a) 1 ABC edge

(b) 2 ABC edges

Figure 4.7: Propagative wave benchmark with square boundary: relative L^2-error w.r.t. P with $\alpha = \pi/4$, "full" basis and several B.C.

As before, we only have to analyse the part of the plots in Fig. 4.7 related to $P \leq 55$, that is when the matrix $(M - E)$ of the linear system (3.3.1) is not ill-conditioned. We can observe that increasing the order of the Padé approximation, we are able to retrieve a smaller and smaller error until a certain threshold, that is the one established by the error obtained in the sqrt case. Once the sqrt-threshold is achieved, it is no longer possible to decrease the error, indeed Padé approximates the exact formulation of the ABC given by sqrt.

The threshold for $\alpha = \pi/4$ is given by $N = 3$, but it has been verified by further simulations that increasing α requires a higher value of the order of Padé approximation N. This is reasonable because, in case 1, increasing the value of α, we get a worse approximation of the ABC, that we recall it is exact only when $\alpha = 0$.

A similar and even better behaviour is observable also picking an appropriate "half" and "quarter" basis, as shown below respectively in the plots in Fig. 4.8.

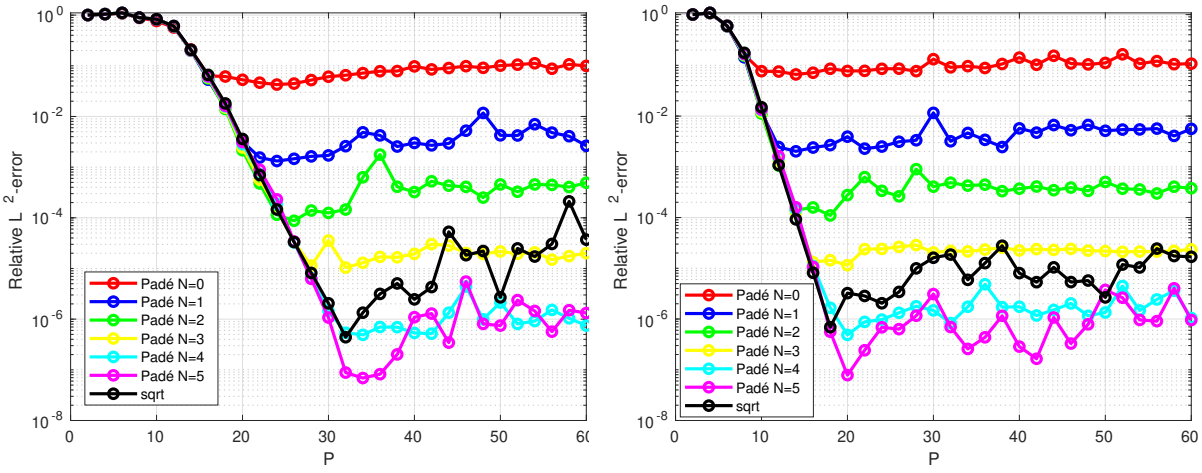

(a) 1 ABC edge, "half" basis

(b) 2 ABC edges, "quarter" basis

Figure 4.8: Propagative wave benchmark with square boundary: relative L^2-error w.r.t. P with $\alpha = \pi/4$ and several B.C.

5 | Numerical results

In order to validate and study the Ultra Weak Variational Formulation with Absorbing Boundary Conditions, we present some numerical results. In Section 5.1, the results concerning a simple benchmark with zeroth-order Absorbing Boundary Condition are shown. In Section 5.2, we present the results regarding a scattering benchmark with square boundary. In Section 5.3, we consider a scattering benchmark with curved boundary. Lastly, in Section 5.4, we take into account two scattering benchmarks with complex boundary.

Notice that whenever the plot of an exact or numerical solution is shown, it is meant to be its real part, since remarks can be equivalently made looking at either the real and imaginary part.

5.1. Validation of the implementation

In order to validate the MATLAB implementation of the method, we first consider a simple benchmark with zeroth-order ABC.

In particular, we want to solve problem (1.1.2) in a square domain $\Omega = (0,1)\times(0,1)$, where the Absorbing Boundary Condition is written in terms of a zeroth-order approximation, namely (1.2.2). Hence, the problem we consider is the following

$$\begin{cases} \Delta u + \kappa^2 u = 0, & \boldsymbol{x} \in \Omega, \\ \partial_{\boldsymbol{n}} u - \imath\kappa u = g, & \boldsymbol{x} \in \partial\Omega. \end{cases} \tag{5.1.1}$$

The function $u^{\text{ref}}(\boldsymbol{x}) = e^{\imath\kappa(\widehat{\boldsymbol{d}}\cdot\boldsymbol{x})}$, $\widehat{\boldsymbol{d}} = (\cos\alpha, \sin\alpha)^T, \alpha \in [0, 2\pi]$ is a manufactured solution of problem (5.1.1) for a particular g that can be retrieved by plugging u^{ref} into the second equation of (5.1.1), that is $g = \partial_{\boldsymbol{n}} u^{\text{ref}} - \imath\kappa u^{\text{ref}}$. In the following, we pick $\alpha = \pi/6$ and $\kappa = 2\pi$. The square domain is meshed with triangular elements and we take into account structured meshes at first and unstructured meshes later.

5.1.1. Validation with structured meshes

First we consider a structured mesh of $K = 18$ triangular elements, as it is shown below in Fig. 5.1.

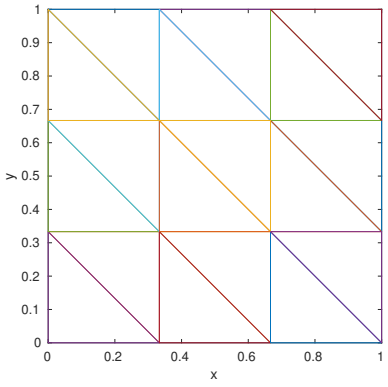

Figure 5.1: Propagative wave benchmark with square boundary: structured mesh $\mathcal{T}$.

For each element of the triangulation, we fix $P = 5$, that is the numerical solution is going to be written as linear combination of 5 waves propagating along 5 equally spaced directions. In order to validate the code, we study a first case in which the shift is equal to the inclination angle of the exact solution, that is $\theta_1 = \alpha = \pi/6$. The matrices M and E have dimension $\dim(M) = \dim(E) = (40, 40)$, while the vector c has dimension $\dim(c) = 40$. The results are shown in Fig. 5.2.

The numerical solution turns out to be exact whenever the shift is equal to the inclination angle of the exact solution, that is the solution vector has all the components equal to 0 except the one which is related to the shape function that is aligned with the exact solution which gains the value 1. Therefore, the output of the code is the one we expected.

If we pick a shift which is not equal to the inclination angle of the exact solution, the numerical solution is not exact anymore, hence the solution vector has its highest component, which is close to 1, related to the closest direction to that of the exact solution, while the other components are much smaller, but not null. Slightly increasing the number of basis functions to $P = 7$, the results quickly improve. In Fig. 5.3, there are the results concerning the case $\theta_1 = 0$ with $P = 5$ and $P = 7$.

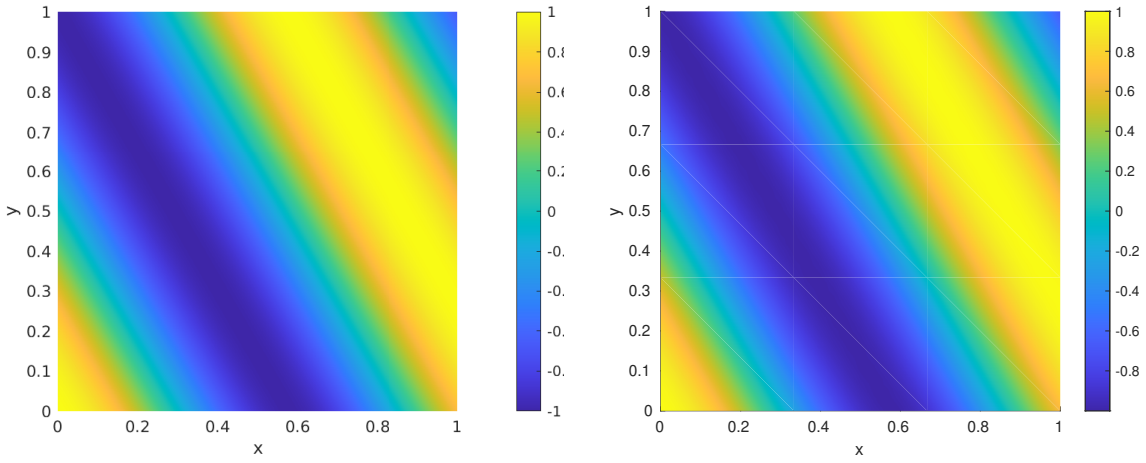

(a) Exact solution, $\alpha = \pi/6$ (b) Numerical solution, $\theta_1 = \pi/6, P = 5$

Figure 5.2: Propagative wave benchmark with square boundary and structured mesh.

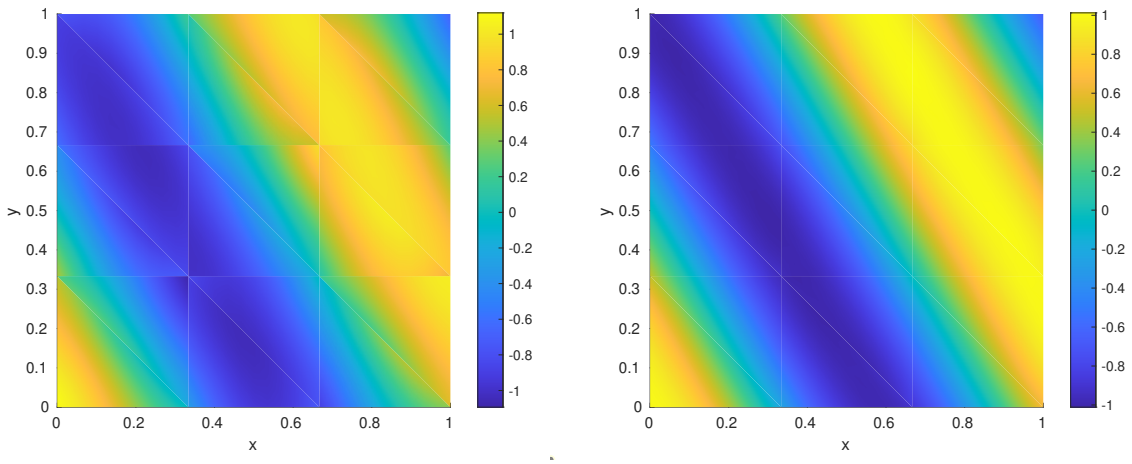

(a) Numerical solution, $\theta_1 = 0, P = 5$ (b) Numerical solution, $\theta_1 = 0, P = 7$

Figure 5.3: Propagative wave benchmark with square boundary and structured mesh.

In order to understand in a deeper way the behaviour of the numerical solution with respect to the number of basis functions, we complete the analysis defining and computing the L^2-error. Denoting by u^{ref} and u^P respectively the exact solution and the numerical one, we consider again the relative L^2-error

$$\epsilon = \frac{||u^{\text{ref}} - u^P||_{L^2(\Omega)}}{||u^{\text{ref}}||_{L^2(\Omega)}}.$$

Observe that all the results that follow exploit a quadrature formula to compute the integral, hence it is not computed exactly, but numerically. Moreover, we write down the conditioning number of the matrix $(M - E)$ to study its ill-conditioning.

In Fig. 5.4, we show the table with the conditioning number and the L^2-error with respect to the number of basis functions P and the plot with the L^2-error with respect to P in logarithmic scale

P	cond(M-E)	L^2-error
1	8.35e+00	4.52e-01
2	9.27e+00	4.53e-01
4	1.84e+01	2.33e-01
8	9.89e+03	3.07e-03
12	1.04e+08	2.44e-13
16	4.68e+12	1.51e-07
20	3.89e+17	4.57e-09
24	8.93e+18	1.61e-08
28	1.56e+19	2.17e-08
32	5.79e+18	1.94e-08

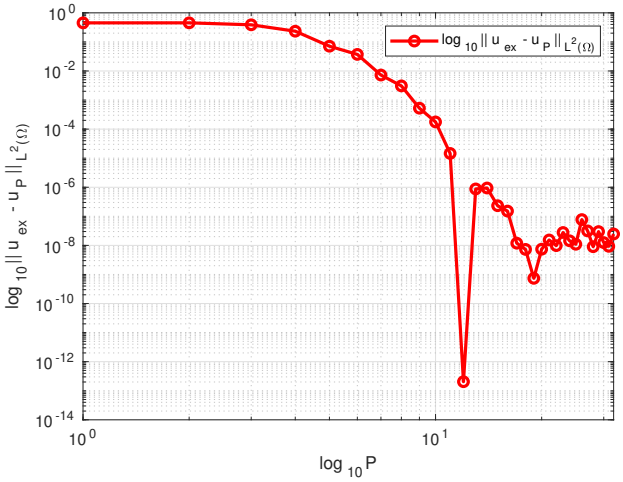

Figure 5.4: Propagative wave benchmark with square boundary and structured mesh: condition number and relative L^2-error w.r.t. P.

Simulations show that the code perfectly works for $P \leq 16$, while taking $P \geq 17$, the results quickly deteriorate and that is related to the fact that the matrix of the linear system $M-E$ is ill-conditioned. Notice that the conditioning number of the matrix $M-E$ does not only depend on the number of basis functions P, but also on the wave-number κ, indeed a higher conditioning number is associated to a higher value of the wave-number κ. Observing the previous table, it is possible to notice that the conditioning number of the matrix $(M - E)$ increases by increasing the number of basis functions and this fact shows that the matrix $(M - E)$ is ill-conditioned. In the second part of [36], some methods that deal with this problem are presented. In particular, a block preconditioning method based on a Singular Value Decomposition (SVD) and another one based on a QR decomposition are analyzed.

Moreover, we can observe in the L^2-error plot that the L^2-error generally decreases by increasing the number of basis functions. The value associated to $P = 12$ seems to be anomalous, but actually in such a case the basis function associated to θ_2 is aligned to the exact solution, hence the numerical solution turns out to be exact and the L^2-error is very small (*a priori* it should be zero, but we find a small non null error, because of the quadrature formula). Also in the case $P = 24$, the alignment between a basis function and the exact solution takes place, in particular we have that $\alpha = \theta_3 = \pi/6$, nevertheless the error is not as low as in the previous case because the conditioning number is very high and the solution of the linear system is affected and damaged.

Lastly, let us observe that once P is picked big enough, it is not possible to further reduce the error because of MATLAB accuracy, indeed the L^2-error stabilizes around the value of 10^{-8} which is the square of MATLAB machine epsilon. This remark lets us choose a good value of P which is not too big, but that it is able to retrieve a small error at the same time, in this case it could be chosen $P = 13$.

5.1.2. Validation with unstructured meshes

We now consider the same problem, but we exploit an unstructured mesh of $K = 68$ triangular elements with mesh size $h = 0.2$ as it is shown below in Fig. 5.5.

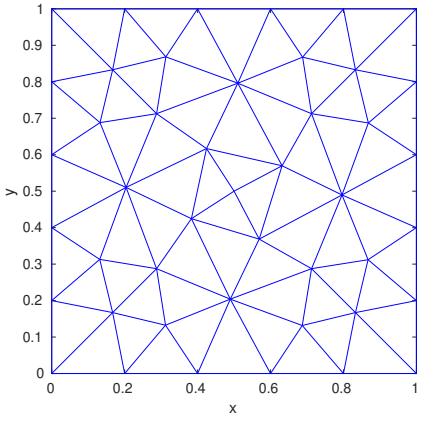

Figure 5.5: Propagative wave benchmark with square boundary: unstructured mesh $\mathcal{T}$.

We fix $\theta_1 = 0$ and we study the behaviour of the numerical solution in the cases $P = 4$ and $P = 5$. In Fig. 5.6, there are the related plots and we can observe that, by increasing the number of shape functions by only 1, the numerical solution gets much better.

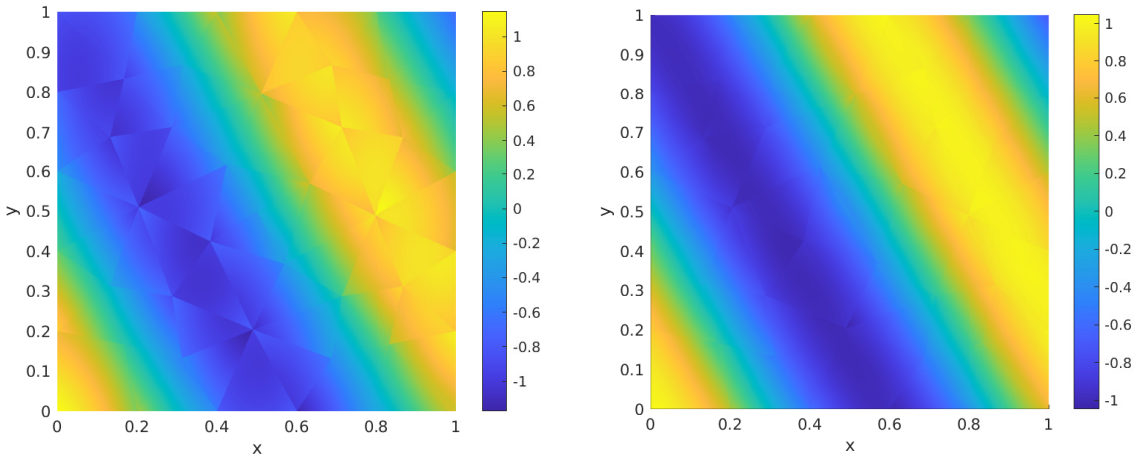

(a) Numerical solution, $\theta_1 = 0, P = 4$ (b) Numerical solution, $\theta_1 = 0, P = 5$

Figure 5.6: Propagative wave benchmark with square boundary and unstructured mesh.

We repeat the analysis concerning the conditioning number of the matrix $(M-E)$ and the L^2-error and we find out that the behaviour is similar to the structured mesh case. Here below in Fig. 5.7, we show the table with the conditioning number and the L^2-error with respect to the number of basis functions P and the plot with the L^2-error with respect to P in logarithmic scale.

P	cond(M-E)	L^2-error
1	2.86e+01	4.06e-01
2	3.55e+01	4.10e-01
4	1.07e+03	3.73e-02
8	1.41e+08	5.26e-05
12	3.32e+14	4.38e-09
16	1.99e+19	7.59e-08
20	1.69e+19	2.27e-07
24	2.84e+19	6.53e-07
28	7.59e+19	8.98e-07
32	3.48e+19	1.93e-07

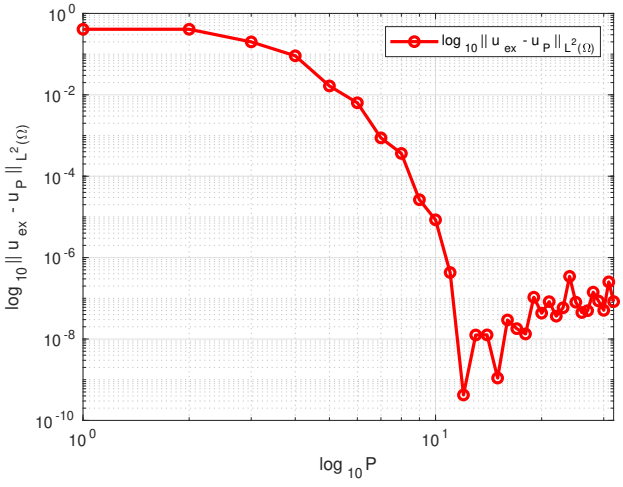

Figure 5.7: Propagative wave benchmark with square boundary and unstructured mesh: condition number and relative L^2-error w.r.t. P.

5.2. Study with a truncated square domain

Now, we consider a classic reference benchmark, that is the scattering of a plane wave by a circular cylinder. The computational domain is a square with a circular hole placed in its center, that is $\Omega = \Omega_{\text{square}} \setminus \Omega_{\text{circle}} = (-1.2, 1.2) \times (-1.2, 1.2) \setminus \{(x, y) \in \mathbb{R}^2 : x^2 + y^2 \leq 1\}$. The scattering of the incident plane wave $u^{\text{inc}}(\boldsymbol{x}) = e^{\imath\kappa \boldsymbol{k}\cdot\boldsymbol{x}}$ with propagation direction $\boldsymbol{k} = (1, 0)$, wave-number $\kappa = 20$, by the circular cylinder of radius R centered at the origin generates the scattered field

$$u^{\text{ref}}(r, \theta) = -\sum_{m=0}^{\infty} \epsilon_m \imath^m \frac{J'_m(\kappa R)}{H^{(1)'}_m(\kappa R)} H^{(1)}_m(\kappa r) \cos(m\theta), r \geq R,$$

where (r, θ) are the polar coordinates, J_m is the mth order Bessel's function, $H^{(1)}_m$ is the mth-order first-kind Hankel function, and ϵ_m is the Neumann function which is equal to 1 for $m = 0$ and 2 otherwise. ABCs are prescribed on the edges of the square and the following Neumann boundary condition (sound-hard case) is prescribed on the boundary of the inner disk

$$\partial_{\boldsymbol{n}} u|_{\partial\Omega_{\text{circle}}} = -\partial_{\boldsymbol{n}} u^{\text{inc}}|_{\partial\Omega_{\text{circle}}}.$$

First, we consider an unstructured mesh of $K = 664$ triangular elements with mesh size $h = 0.1$, as shown in Fig. 5.8.

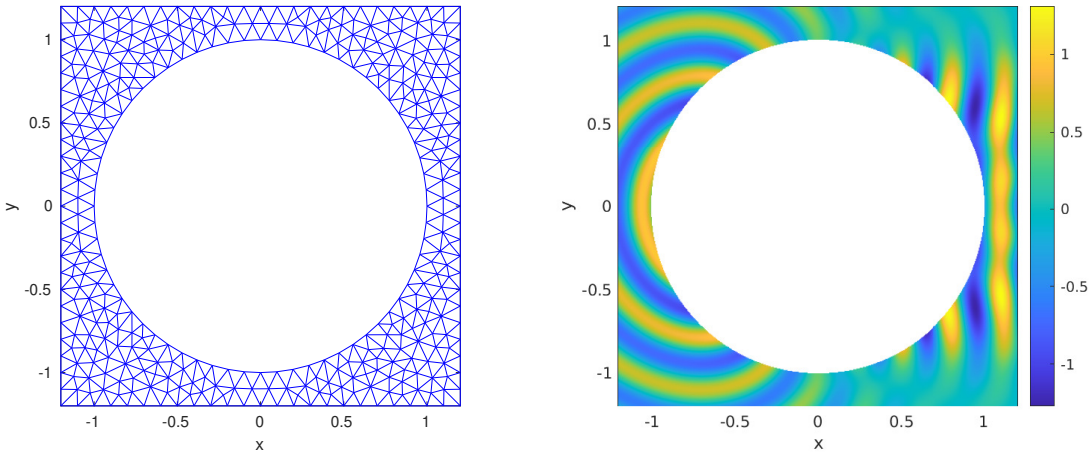

(a) Mesh $\mathcal{T}$ (b) Exact solution

Figure 5.8: Scattering benchmark with square boundary.

We start fixing the number of basis functions $P = 8$, null shift that is $\theta_1 = 0$ and taking into consideration the $\imath\kappa$ and sqrt cases. In Fig. 5.9 and Fig 5.10, we report the numerical solutions and the computed errors that show a good behaviour of the numerical solution in botch cases.

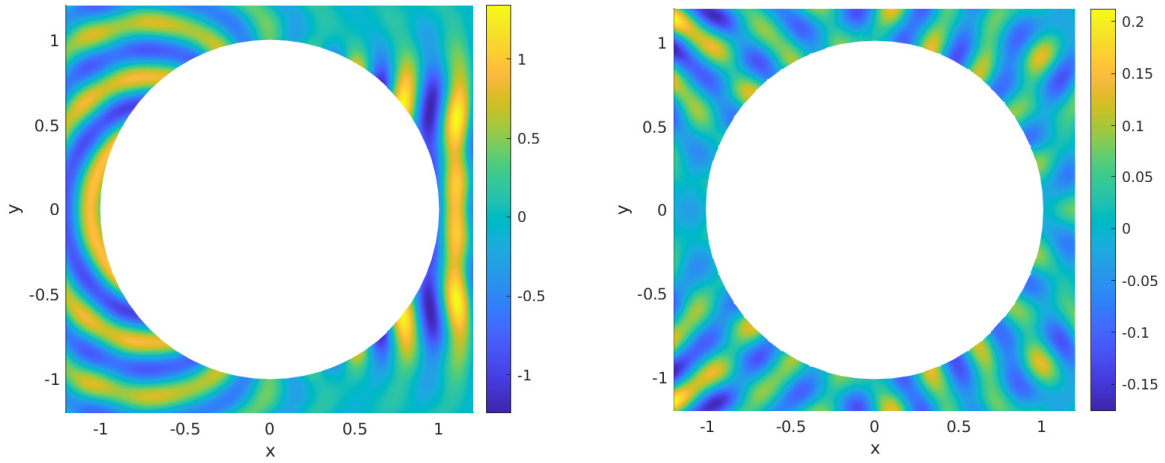

(a) Numerical solution

(b) Error $\mathfrak{Re}(u^{\text{num}} - u^{\text{ref}})$

Figure 5.9: Scattering benchmark with square boundary: $\imath\kappa$.

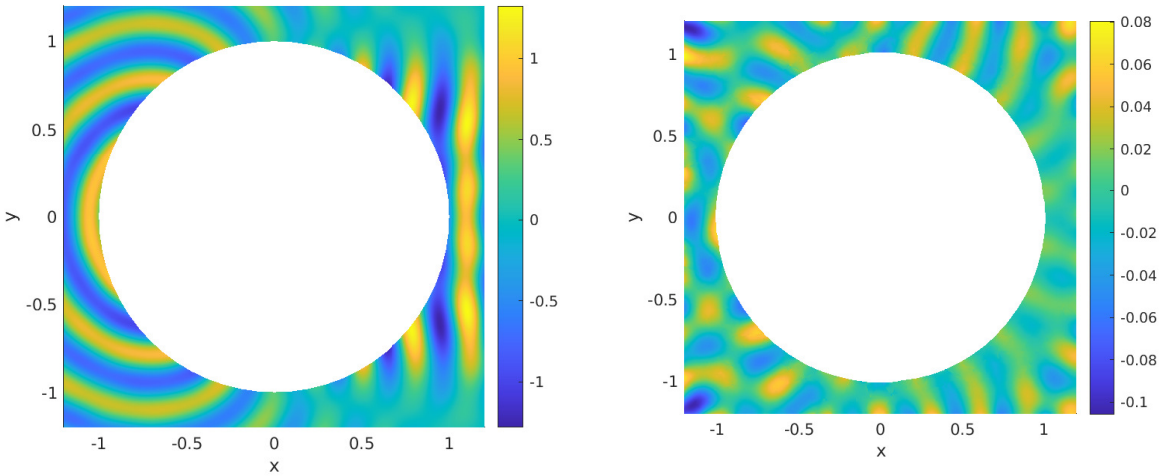

(a) Numerical solution

(b) Error $\mathfrak{Re}(u^{\text{num}} - u^{\text{ref}})$

Figure 5.10: Scattering benchmark with square boundary: sqrt.

We proceed studying the behaviour of the relative L^2-error with respect to the density of the mesh measured as $\sqrt{\#\text{nodes}}$, that is an h-refinement with $P = 8$ and with respect to the cardinality of the set of shape functions, that is a p-refinement with $h = 0.1$. The two plots are shown here below in Fig 5.11. In each plot, we display the best approximation error and the numerical error related to the $\imath\kappa$ and sqrt cases

$$\frac{||u^{\text{num}} - u^{\text{ref}}||_{L^2(\Omega)}}{||u^{\text{ref}}||_{L^2(\Omega)}}.$$

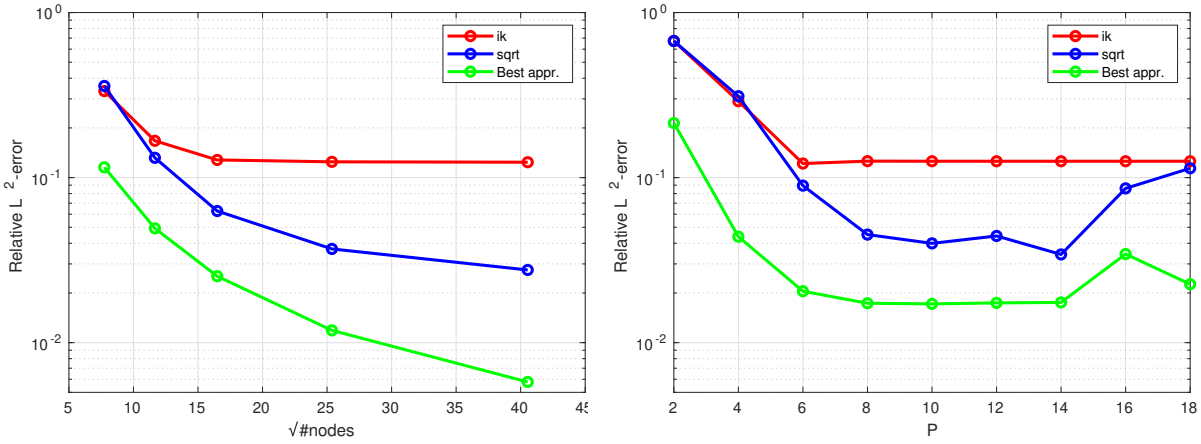

(a) h-refinement, $P = 8$ (b) p-refinement, $h = 0.1$

Figure 5.11: Scattering benchmark with square boundary: refinements.

The results obtained by the use of the exact computation of the ABC are better than those related to the zeroth-order approximation. Nevertheless, they are worse than the best approximation. Moreover, as it is possible to observe in the right side of the second plot, if the number of basis function P is too big, conditioning problems arise and deteriorate the numerical solution. Same consideration can be retrieved for the h-refinement which manifests harsh instability after a certain threshold of the mesh size that consequently cannot be too small. The numerical error is not close to the best approximation one and, contrary to the once-cell case, the use of a "half" basis in the boundary elements does not lead to a significant improving.

We proceed by showing the results that compare the two refinements in the case of Padé with $\phi = 0$ and sqrt.

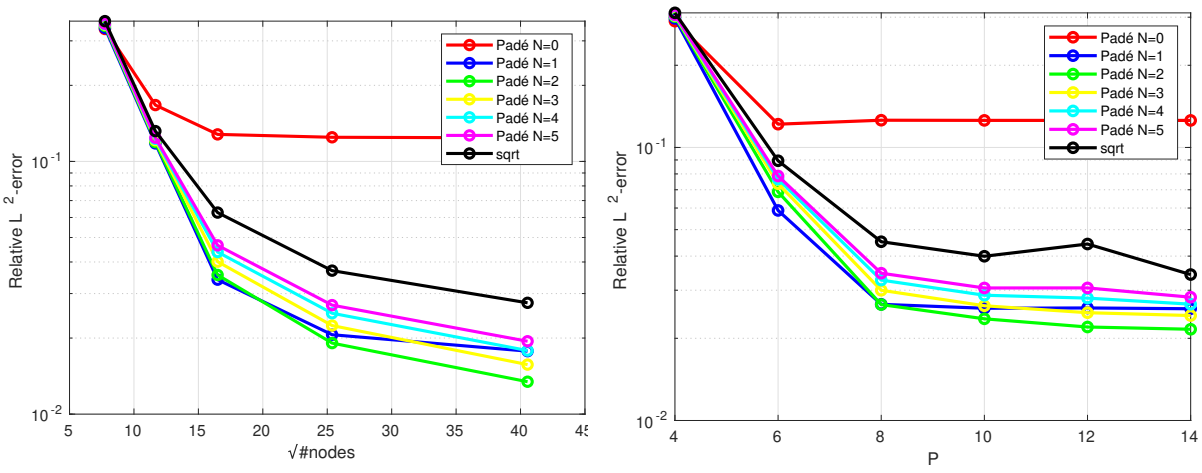

(a) h-refinement, $P = 8$

(b) p-refinement, $h = 0.1$

Figure 5.12: Scattering benchmark with square boundary: refinements.

What we can observe from the plots in Fig. 5.12 is that, refining the mesh or enriching the set of basis functions, the numerical error decreases in all cases and is led to a plateau. Moreover, for $N \geq 1$ the numerical error is close to the one of the sqrt case.

Lastly, a problem concerning Padé approximation arises, indeed we expected the error to decrease in a significant way increasing the order of the approximation N and the plots above do not show the expected behaviour. It may be caused by a combination of different sources of error:

- Modeling error: no corner treatment has been taken into account.
- Conditioning: it leads to the deterioration of the numerical solution.
- Numerical error: related to the numerical scheme we use.

To dig the issue, in Fig. 5.13, the error plots are displayed and made available to comparison. Nevertheless, no important conclusion can be retrieved, indeed it is not evident any particular anomaly in the corner areas.

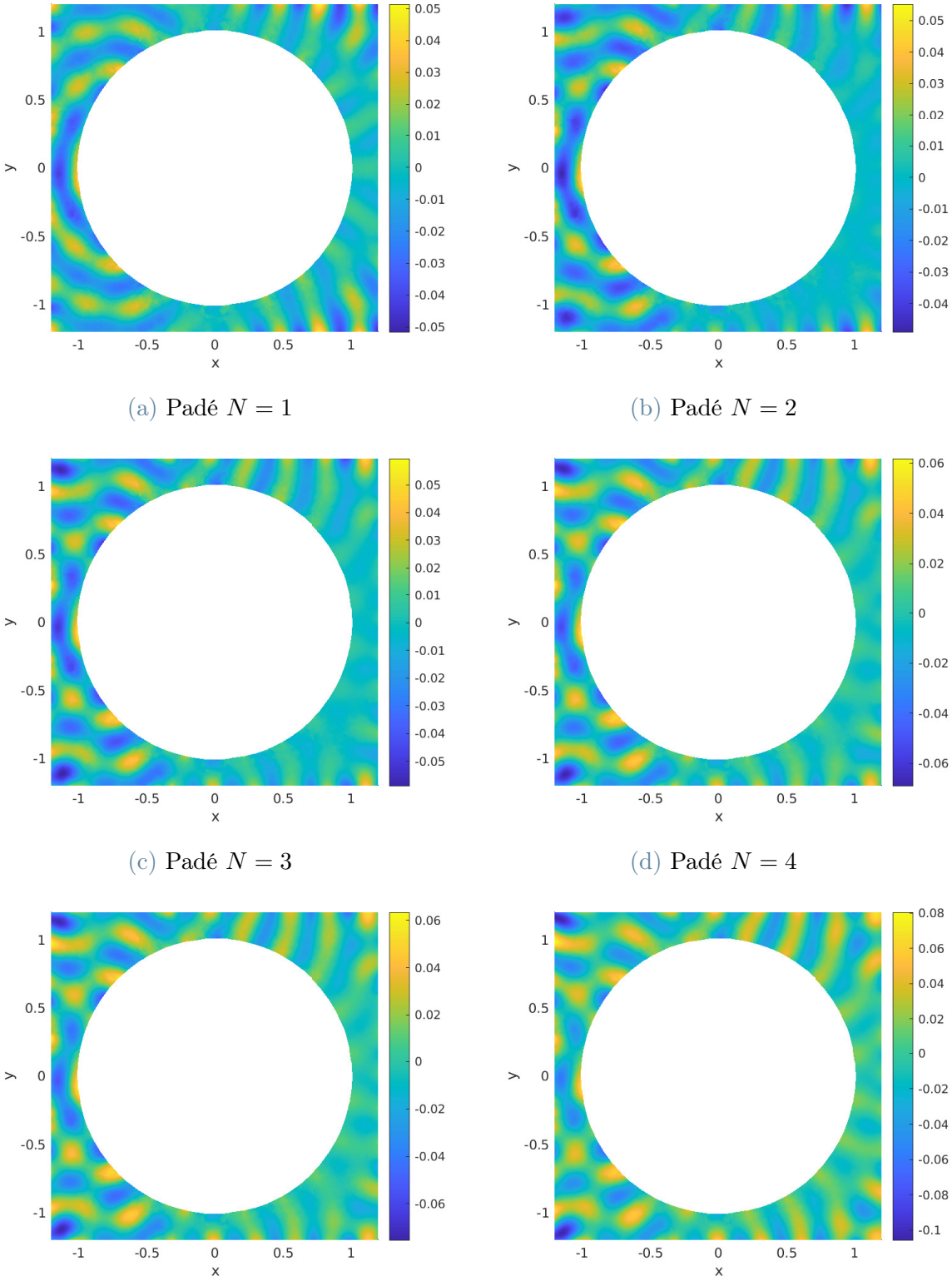

(a) Padé $N = 1$

(b) Padé $N = 2$

(c) Padé $N = 3$

(d) Padé $N = 4$

(e) Padé $N = 5$

(f) sqrt

Figure 5.13: Scattering benchmark with square domain: error $\mathfrak{Re}(u^{\text{num}} - u^{\text{ref}})$.

5.3. Investigation with a truncated circular domain

This example, as the previous one, deals with the scattering of a plane wave by a circular cylinder. We consider the same solution and the same parameters, but the domain we take into account is an annulus $\Omega = \{(x, y) \in \mathbb{R}^2 : R_1^2 < x^2 + y^2 < R_2^2, R_1 = 0.5, R_2 = 1\}$. ABCs are prescribed on the external boundary of the domain and a non-homogeneous Neumann boundary condition is prescribed on the inner boundary of the domain in the same form as the one in the previous section.

We take into consideration this benchmark because we know that the boundary condition (1.2.3) with the DtN operator (1.2.4) is exact only for straight boundaries, so we are interested in observing its behaviour in the case of curved boundaries.

First, we take an unstructured mesh of $K = 2306$ triangular elements with mesh size $h = 0.05$, as shown in Fig. 5.14.

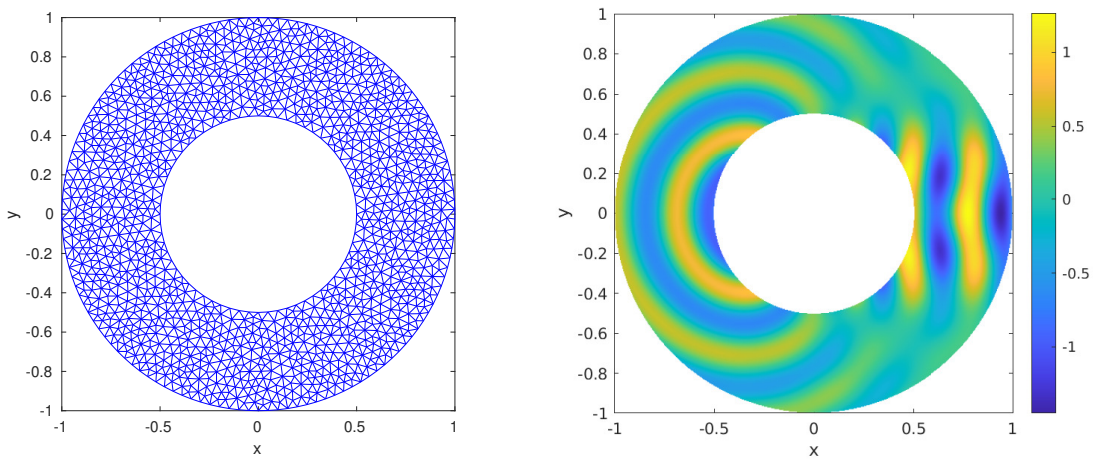

(a) Mesh $\mathcal{T}$ (b) Exact solution

Figure 5.14: Scattering benchmark with curved boundary.

We proceed as we did in the previous benchmark: after checking the behaviour of the numerical method, first we consider the $\imath\kappa$ and sqrt cases and compare them with respect to the h and p refinements. Then we conclude with the same comparison between the sqrt and Padé case.

We start fixing the number of basis functions $P = 8$, null shift that is $\theta_1 = 0$ and taking into consideration the $\imath\kappa$ and sqrt case. In Fig. 5.15 and Fig 5.16 we show the numerical solutions and the computed errors. Observing the range of the error, we can claim a better behaviour of the sqrt case with respect to the $\imath\kappa$ one and no particular issues concerning the areas close to the absorbing boundary.

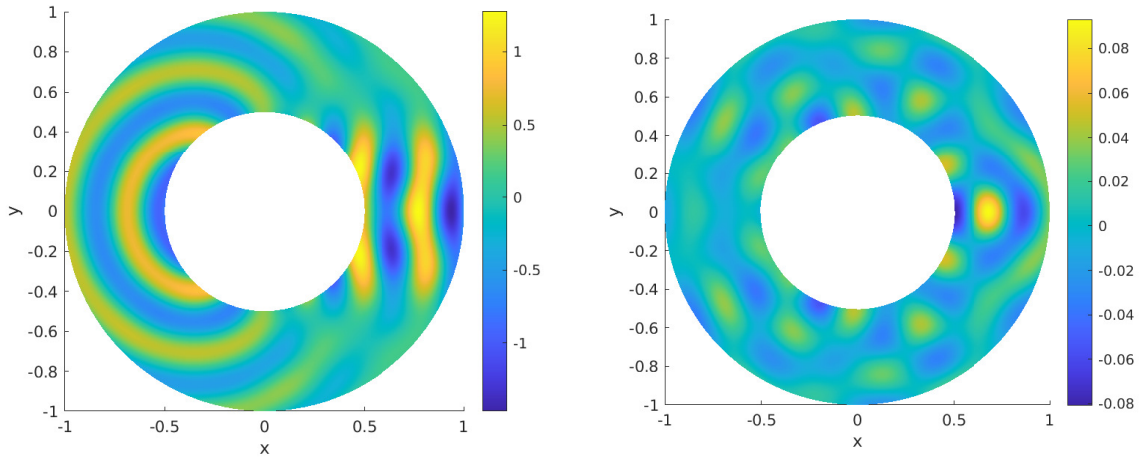

(a) Numerical solution

(b) Error $\mathfrak{Re}(u^{\text{num}} - u^{\text{ref}})$

Figure 5.15: Scattering benchmark with curved boundary: $\imath\kappa$.

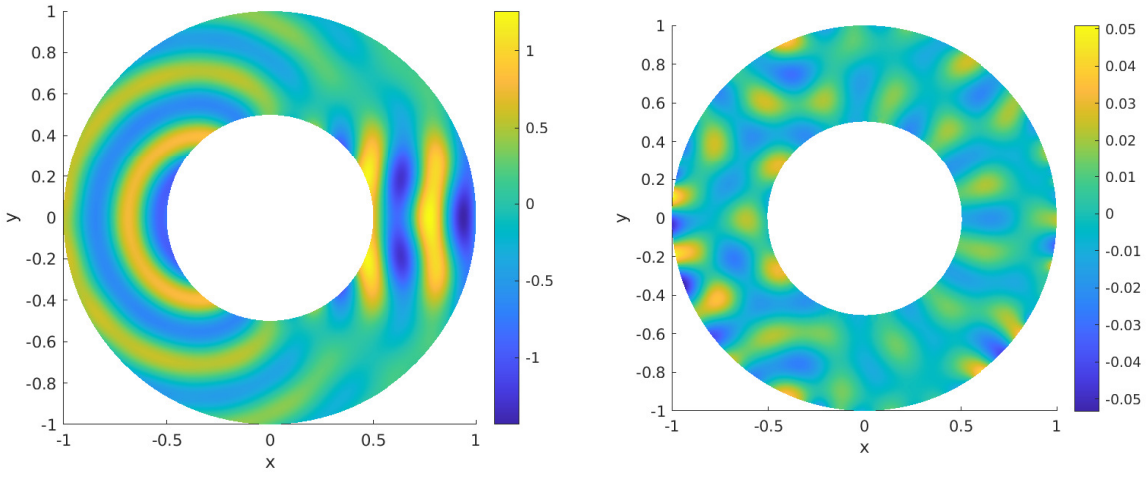

(a) Numerical solution

(b) Error $\mathfrak{Re}(u^{\text{num}} - u^{\text{ref}})$

Figure 5.16: Scattering benchmark with curved boundary: sqrt.

Once again, we proceed studying the behaviour of the relative L^2-error with respect to the density of the mesh measured as $\sqrt{\#\text{nodes}}$, that is an h-refinement with $P = 8$ and with respect to the cardinality of the set of shape functions, that is a p-refinement with $h = 0.1$. The plots are shown here below in Fig 5.17 and Fig. 5.18.

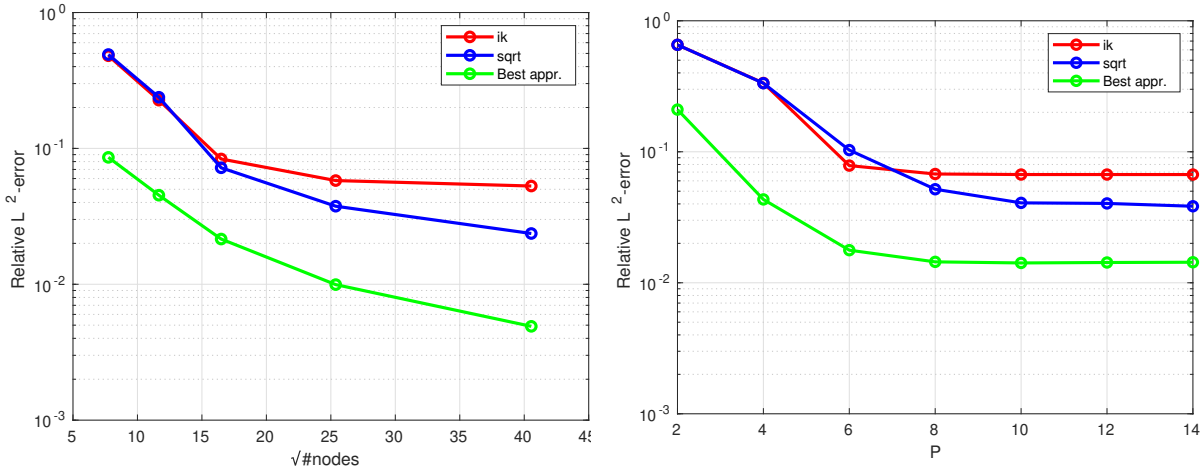

(a) h-refinement, $P = 8$ (b) p-refinement, $h = 0.1$

Figure 5.17: Scattering benchmark with curved boundary: refinements.

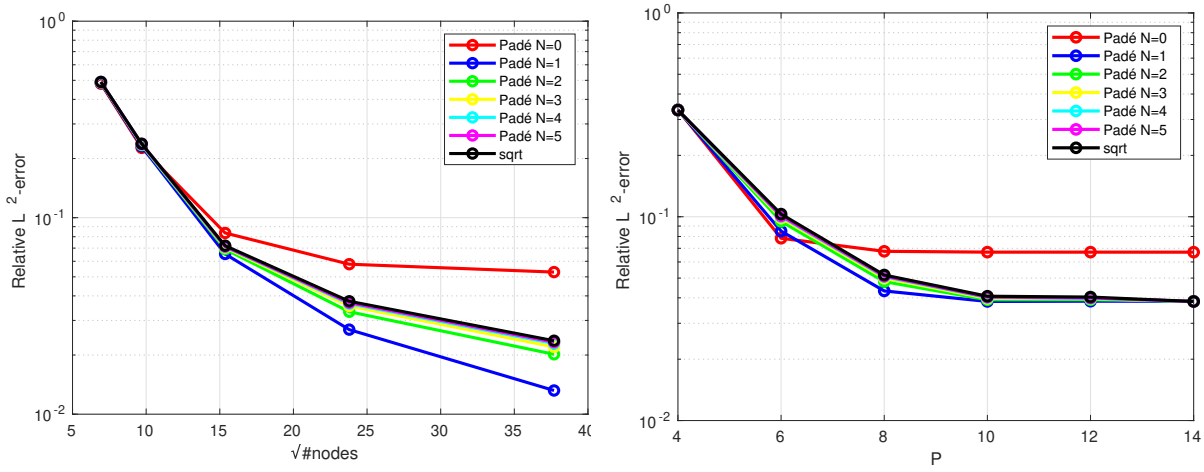

(a) h-refinement, $P = 8$ (b) p-refinement, $h = 0.1$

Figure 5.18: Scattering benchmark with curved boundary: refinements.

The numerical error related to the sqrt case is not close to the best approximation and for $N \geq 1$ the numerical error is close to the one of the sqrt case. We know that an additional modeling error is present here because the sqrt is not exact for curved boundaries.

As we explained in Section 1.2.4, there exists a modified form of the ABC that holds in the case of regular curved boundaries and, in particular, in two dimensions for a regular planar curve $\Gamma \subset \mathbb{R}^2$ it takes into account, besides a term that descritize the usual exact ABC for planar boundaries as presented in Prop. 3.1, also a second additional term (3.3.5) that deals with the curved boundary and where, in this example, the curvature is such that $\gamma = 1/R_2$. We carried out some simulations to verify the behavior of the numerical solution in the case of the improved absorbing boundary condition and the results are shown below in Fig. 5.19 and Fig. 5.20.

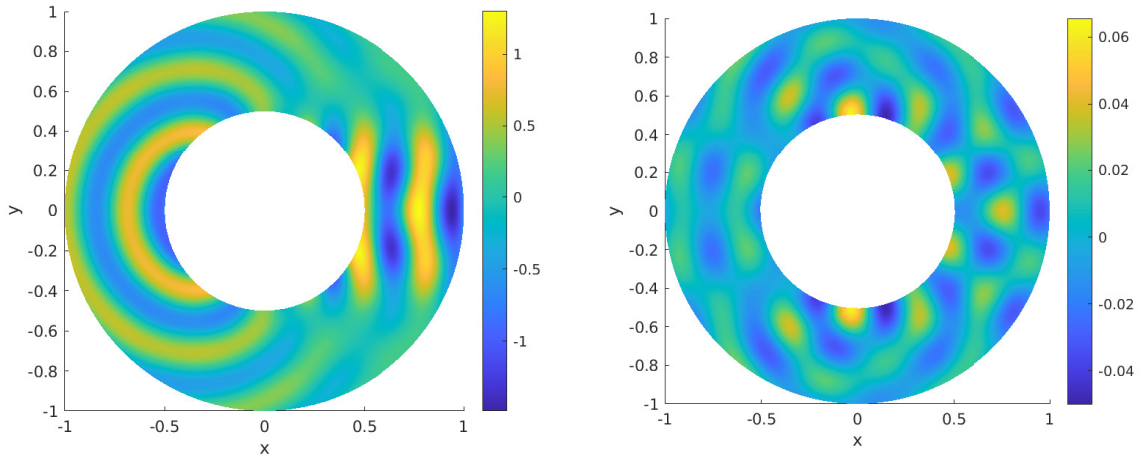

(a) Numerical solution

(b) Error $\mathfrak{Re}(u^{\text{num}} - u^{\text{ref}})$

Figure 5.19: Scattering benchmark with curved boundary: $\imath\kappa$.

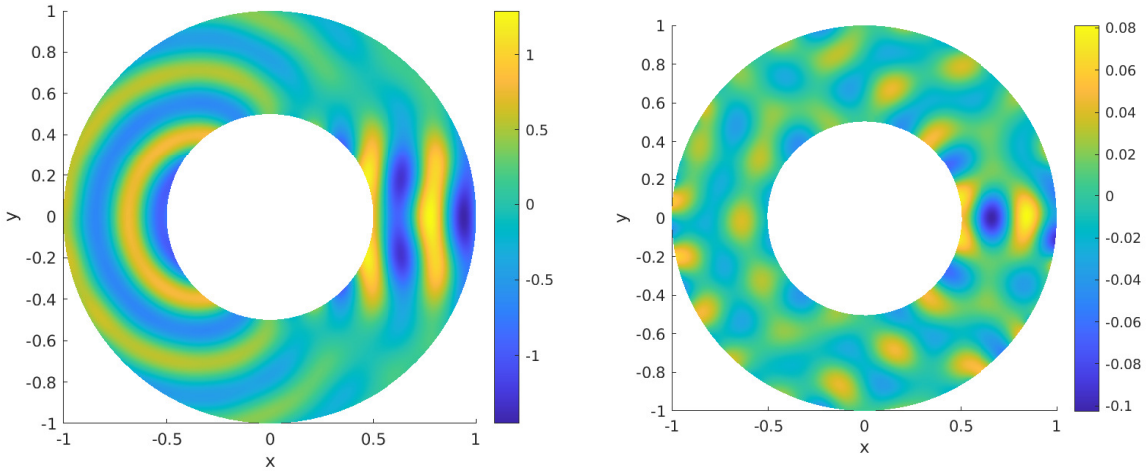

(a) Numerical solution

(b) Error $\mathfrak{Re}(u^{\text{num}} - u^{\text{ref}})$

Figure 5.20: Scattering benchmark with curved boundary: sqrt.

Observing the error plot in Fig. 5.19 and comparing it to the one in Fig. 5.15, we can claim a better behavior of the numerical solution since the range of the error is smaller. Nevertheless, we can not see any improvement comparing the error plot in Fig. 5.16 and the one in Fig. 5.20, and, on the contrary, we can note a deterioration. This is surprising because in the case of standard polynomial FEM relevant improving has been shown.

5.4. Illustration of applications

In this very last section, we take into account numerical experiments that deal with the scattering problem by obstacles whose geometry is complex. In particular, we consider the scattering of a plane wave first by an aircraft and then by two squares.

We limit ourselves to simulations of the numerical scheme by sqrt and comment the plots relatively to the numerical solution, being the exact one not available.

The domain we consider for the example with the aircraft is $\Omega = (-4,7)\times(-4,4)\setminus\Omega_{\text{aircfraft}}$. The scattering of the plane wave solution $u^{\text{inc}}(\boldsymbol{x}) = e^{\imath\kappa\boldsymbol{k}\cdot\boldsymbol{x}}$ with propagation direction $\boldsymbol{k} = (1,0)$, wave-number $\kappa = 20$, by the aircraft generates a scattered field that can not be represented in a closed form as easily as before, because of the complexity of the obstacle. As before, ABCs are prescribed on the external boundary of the domain and a non-homogeneous Neumann boundary condition is prescribed on the boundary of the aircraft. We take an unstructured mesh of $K = 4316$ triangular elements with mesh size $h = 0.05$.

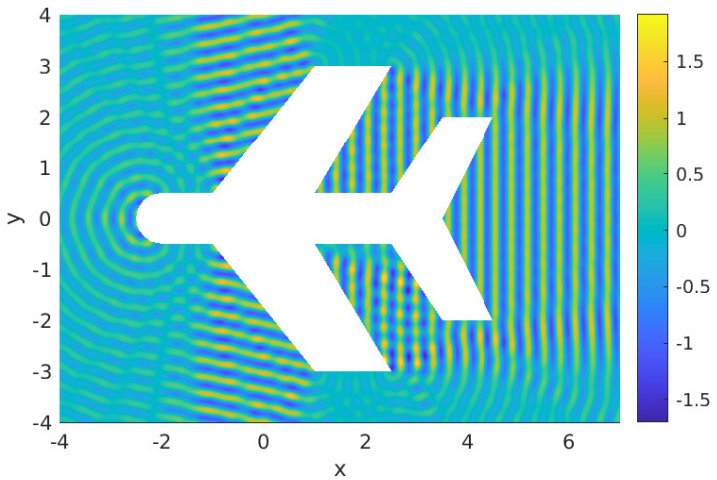

Figure 5.21: Scattering benchmark with aircraft: numerical solution.

The domain we consider for the example with square boundary containing two square scatterers is $\Omega = (-1,4)\times(-2,3)\setminus([0,1]\times[0,1]\cup[2,3]\times[0,1])$. Once again, the scattering of the plane wave solution $u^{\text{inc}}(\boldsymbol{x}) = e^{\imath\kappa\boldsymbol{k}\cdot\boldsymbol{x}}$ with propagation direction $\boldsymbol{k} = (\sqrt{2}/2, \sqrt{2}/2)$, wave-number $\kappa = 20$, by the two obstacles generates a scattered field that can not be represented in a closed form. ABCs are prescribed on the external boundary of the domain and a non-homogeneous Neumann boundary condition is prescribed on the boundary of the fissures. We take an unstructured mesh of $K = 1698$ triangular elements with mesh size $h = 0.1$.

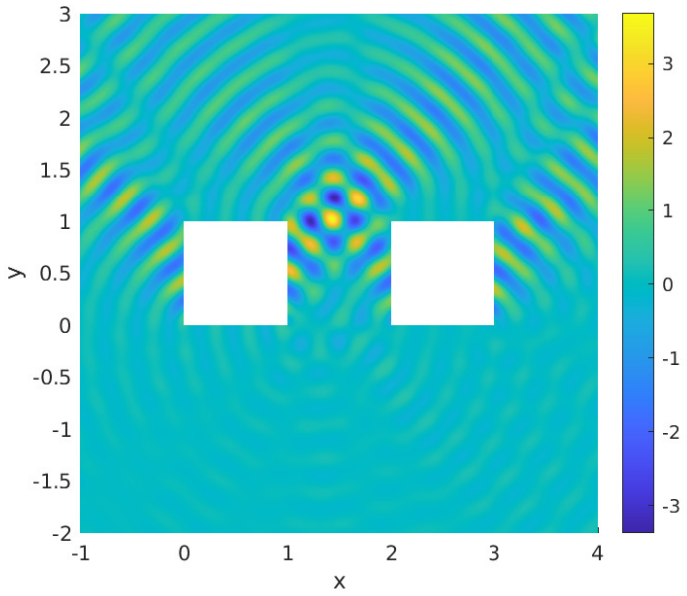

Figure 5.22: Scattering benchmark with two fissures: numerical solution.

Observing the two numerical solutions reported in Fig. 5.21 and Fig. 5.22 respectively, we can claim a good behaviour of the numerical scheme even in the case of non-trivial geometries. Indeed, in the first case we can observe a wave-shadow which is typically recurrent in similar examples with aircraft-shape scatterer, while in the second case we can observe a numerical solution which is analogous to the one obtained in [50] in a similar experiment. This allows the extension of the study to every scenario in the two dimensional framework with very little effort in the code: indeed it is enough to import the mesh associated to the benchmark to which we want to carry experiments on paying attention to the tag associated to the edges which lay onto the boundary for a correct treatment of the boundary conditions.

Conclusions

We have investigated the combination of the Ultra Weak Variational Formulation with Absorbing Boundary Conditions in the framework of a Trefftz method applied to the Helmholtz equation. In particular, we have provided a new formulation and we have implemented a finite element solver to perform numerical simulations.

Main results and remarks

First of all, the simulations performed in the one-cell numerical domain show a better behaviour of the absorbing boundary condition when it is expressed by the sqrt form rather than its zeroth-order approximation $\imath\kappa$. Moreover, directional adaptivity turns out to be very effective in improving the results. Indeed, once it is applied to either the sqrt form and the high-order Padé approximation in a proper way, we can recover results that are very similar to the ones obtained by projection. The Padé approximation behaves in the correct way: increasing the order N of the approximation, we get better and better results that tend to the ones obtained by sqrt.

The simulations performed in the multi-cell numerical domain keep on showing a better behaviour of the absorbing boundary condition when it is expressed by the sqrt form rather than its zeroth-order approximation $\imath\kappa$. Nevertheless, directional adaptivity does not turn out to be effective, therefore we can not obtain by sqrt results that are comparable with those obtained by projection. Moreover, the use of Padé approximation presents some issues and unexpected effects. In particular, in the case of approximation of order $N = 1$, the results are better than the ones associated to $N = 0$, while for a bigger value of N, we can not record any significant further improving. However, we can confirm the converging behaviour of the Padé approximation to the exact formulation given by the sqrt with respect to the order N of the approximation.

The observation of the error in the case of rectangular artificial boundary does not let us perceive the necessity of a proper treatment for the corners. Nevertheless, this aspect turned out to be crucial in the case of standard finite element methods with polynomial basis functions.

Lastly, exploiting a proper treatment in the case of curved boundaries consists in an improving only for the $\imath\kappa$ case, while in all the other cases its effect can be neglected. Thus, its formulation may not be suitable for our context.

Challenges and perspective

Because of the remarks we presented in the previous page, further studies should be focused on the behaviour of the Padé approximation of the absorbing boundary condition. Moreover, due to the limit given by the conditioning issues of the linear system, some techniques that deal with them may be tested to get better and clearer results. Directional adaptivity for the multi-cell numerical domain deserves a deeper study and further tests. Eventually, proper treatments concerning the local geometry of the boundary (corners, curved sections) can be explored to understand the precise role they play in the numerical error of the solution.

Bibliography

[1] R.D. Ciskowski, C.A. Brebbia, *Boundary element methods in acoustics*, Computational Mechanics Publications, Southampton; Boston/Elsevier Applied Science, London; New York, 1991

[2] P. Solin, K. Segeth, I. Dolezel, *Higher-Order Finite Element Methods*, Chapman & Hall, 2004

[3] G. Karniadakis, S. Sherwin, *Spectral/hp Element Methods for Computational Fluid Dynamics*, Oxford University Press, 2013

[4] H. Bériot, G. Gabard, E. Perrey-Debain, *Analysis of high-order finite elements for convected wave propagation*, Int. J. Numer. Methods Eng. 96 (11) (2013) 665-688

[5] R. Hiptmair, A. Moiola, I. Perugia, *A survey of Trefftz methods for the Helmholtz equation*, in "Building bridges: connections and challenges in modern approaches to numerical partial differential equations", Springer (2016) 237-279

[6] T. Luostari, T. Huttunen, P. Monk, *The ultra weak formulation using Bessel basis functions*, Commun. Comput. Phys. 11 (2) (2012) 400-414

[7] G. Gabard, *Discontinuous Galerkin methods with plane waves for time-harmonic problems*, J. Comput. Phys. 225 (2007) 1961-1984

[8] J. Caruthers, J. French, G. Raviprakash, *Green function discretization for numerical solution of Helmholtz equation*, J. Sound Vib. 187 (4) (1995) 553-568

[9] A. Lieu, G. Gabard, H. Bériot, *A comparison of high-order polynomial and wave-based methods for Helmholtz problems*, J. Comput. Phys. 321 (2016) 105-125

[10] R. Kechroud, X. Antoine, A. Soulaimani, *Numerical accuracy of a Padé-type non-reflecting boundary condition for the finite element solution of acoustic scattering problems at high-frequency*, Int. J. Numer. Methods Eng. 64 (2005) 1275-1302

[11] K. Schmidt, J. Diaz, C. Heier, *Non-conforming Galerkin finite element methods for local absorbing boundary conditions of higher order*, Comput. Math. Appl. 70 (2015)

2252-2269

[12] E. Turkel, *Boundary conditions and iterative schemes for the Helmholtz equation in unbounded regions*, Comput. Methods Acoust. Probl. (2008) 127-158

[13] A. Bermúdez, L. Hervella-Nieto, A. Prieto, R. Rodríguez, *An optimal perfectly matched layer with unbounded absorbing function for time-harmonic acoustic scattering problems*, J. Comput. Phys. 223 (2007) 469-488

[14] T. Huttunen, J.P. Kaipio, P. Monk, *The perfectly matched layer for the ultra-weak variational formulation of the 3D Helmholtz equation*, Int. J. Numer. Methods Eng. 61 (2004) 1072-1092

[15] E. Turkel, A. Yefet, *Absorbing PML boundary layers for wave-like equations*, Appl. Numer. Math. 27 (1998) 533-557

[16] A. Modave, E. Delhez, C. Geuzaine, *Optimizing perfectly matched layers in discrete contexts*, Int. J. Numer. Methods Eng. 99 (2014) 410-437

[17] I. Harari, M. Slavutin, E.Turkel, *Analytical and numerical studies of a finite element PML for the Helmholtz equation*, J. Comput. Acoust. 8 (2000) 121-137

[18] I. Harari, R. Djellouli, *Analytical study of the effect of wave number on the performance of local absorbing boundary conditions for acoustic scattering*, Appl. Numer. Math. 50 (2004) 15-47

[19] H. Barucq, R. Djellouli, A. Saint-Guirons, *Three-dimensional approximate local DtN boundary conditions for prolate spheroid boundaries*, J. Comput. Appl. Math. 234 (2010) 1810-1816

[20] F. Collino, S. Ghanemi, P. Joly, *Domain Decomposition Method for Harmonic Wave Propagation: a General Presentation*, Comput. Methods Appl. Mech. Engrg. (2000), 184, pp. 171-211

[21] Y. Boubendir, X. Antoine, C. Geuzaine, *A Quasi-Optimal Non-Overlapping Domain Decomposition Algorithm for the Helmholtz Equation*, J. Comput. Phys. (2012), 231 (2), pp. 262-280

[22] A. Modave, A. Royer, X. Antoine, C. Geuzaine, *A non-overlapping domain decomposition method with high-order transmission conditions and cross-point treatment for Helmholtz problems*, Comput. Methods Appl. Mech. Engrg. (2020), 368, 113162

[23] F. Collino, P. Joly, M. Lecouvez, *Exponentially convergent non overlapping domain decomposition methods for the Helmholtz equation*, ESAIM: Mathematical Modelling and

Numerical Analysis, 54(3) (2020) 775-810

[24] C. Farhat, R. Tezaur, J. Toivanen, *A domain decomposition method for discontinuous Galerkin discretizations of Helmholtz problems with plane waves and Lagrange multipliers*, Int. J. Numer. Methods Eng. 78 (2009) 1513-1531

[25] A. Royer, C. Geuzaine, E. Béchet, A. Modave, *A non-overlapping domain decomposition method with perfectly matched layer transmission conditions for the Helhmoltz equation*, Comput. Methods Appl. Mech. Engrg. (2022), 395

[26] A. Modave, T. Chaumont-Frelet, *A hybridizable discontinuous Galerkin method with characteristic variables for Helmholtz problems*, preprint at https://hal.archives-ouvertes.fr/hal-03909368

[27] G. Giorgiani, S. Fernández-Méndez, A. Huerta, *Hybridizable discontinuous Galerkin p-adaptivity for wave propagation problems*, Int. J. Numer. Methods Fluids, 72 (2013) 1244-1262

[28] R. Griesmaier, P. Monk, *Error analysis for a hybridizable discontinuous Galerkin method for the Helmholtz equation*, J. Scient. Comput. 49 (2011) 291-310

[29] B. Engquist, A. Majda, *Absorbing boundary conditions for numerical simulation of waves*, Proc. Natl. Acad. Sci. 74 (1977) 1765-1766

[30] A. Modave, C. Geuzaine, X. Antoine, *Corner treatments for high-order local absorbing boundary conditions in high-frequency acoustic scattering*, J. Comput. Phys. 401 (2020)

[31] F. A. Milinazzo, C. A. Zala, G. H. Brooke, *Rational square-root approximations for parabolic equations algorithms*, J. Acoust. Soc. Am. 101 (1997) 437-459

[32] A. Modave, A. Atle, T. Warburton, *Survey of accurate nonreflective boundary treatments for seismic waves*, Internal report (2017)

[33] R.L. Higdon, *Absorbing boundary conditions for difference approximations to the multidimensional wave equation*, Math. Comput. 47 (1986) 437-459

[34] T. Hagstrom, T. Warburton, *Complete radiation boundary conditions: minimizing the long time error growth of local methods*, SIAM J. Numer. Anal. 47 (2009) 3678-3704

[35] R. Kechroud, X. Antoine, A. Soulaimani, *Numerical accuracy of a Padé-type non-reflecting boundary condition for the finite element solution of acoustic scattering problems at high-frequency*, Int. J. Numer. Methods Eng. 64 (2005) 1275-1302

[36] H. Barucq, A. Bendali, J. Diaz, S. Tordeux, *Local strategies for improving the conditioning of the plane-wave ultra-weak variational formulation*, J. Comput. Phys. 441

(2021)

[37] O. Cessenat, B. Després, *Application of an ultra weak variational formulation of elliptic PDEs to the two-dimensional Helmholtz problem*, J. Comput. Phys. 35 (1998)

[38] C. J. Gittelson, R. Hiptmair, I. Perugia, *Plane wave discontinuous Galerkin methods: Analysis of the h-version*, M2AN Math. Model. Numer. Anal. 43 (2009) 297-331

[39] R. Hiptmair, A. Moiola, I. Perugia, *Plane wave discontinuous Galerkin methods for the 2D Helmholtz equation: analysis of the p-version*, SIAM J. Numer. Anal. 49 (2011) 264-284

[40] S. Congreve, P. Houston, I. Perugia, *Adaptive refinement for hp-version Trefftz discontinuous Galerkin methods for the homogeneous Helmholtz problem*, Adv. Comput. Math. 45 (2019) 361-393

[41] R. Hiptmair, A. Moiola, I. Perugia, Ch. Schwab, *Trefftz-discontinuous Galerkin methods: hp-version and exponential convergence*, Proceedings of Waves 2013 - The 11th International Conference on Mathematical and Numerical Aspects of Waves, Gammarth, Tunisia, June 3-7, (2013) 359-360

[42] W. F. Mitchell, M. A. McClain, *A Comparison of hp-adaptive Strategies for Elliptic Partial Differential Equations*, Technical Report NISTIR 7824 National Institute of Standards and Technology (2011)

[43] A. Moiola, R. Hiptmair, I. Perugia, *Plane wave approximation of homogeneous Helmholtz solutions*, Z. Angew. Math. Phys. 62.5 (2011) 809–837

[44] I. N. Vekua, *New methods for solving elliptic equations*, North Holland (1967)

[45] O. Laghrouche, P. Bettes, R. J. Astley, *Modelling of short wave diffraction problem using approximating systems of plane waves*, Internat. J. Numer. Methods Engrg. 54 (2002) 1501-1533

[46] E. Parolin, D. Huybrechs, A. Moiola, *Stable approximation of Helmholtz solutions by evanescent plane waves*, preprint at arXiv:2202.05658 (2022)

[47] T. Huttunen, P. Monk, J. P. Kaipio, *Computational aspects of the ultra-weak variational formulation*, J. Comput. Phys. 182 (1) (2002) 27-46

[48] T. Huttunen, P. Gamallo, R. Astley, *A comparison of two wave element methods for the Helmholtz problem*, Commun. Numer. Meth. Engrg. 25 (1) (2009) 35-52

[49] S. Congreve, J. Gedicke, I. Perugia, *Numerical investigation of the conditioning for*

plane wave discontinuous Galerkin methods, in European Conference on Numerical Mathematics and Advanced Applications, Springer (2017) 493–500

[50] B. Gilvey, J. Trevelyan, G. Hattori, *Singular enrichment functions for Helmholtz scattering at corner locations using the Boundary Element Method*, Int. J. Numer. Methods Eng. (2017)

List of Figures

1.1 Example of domain 7

2.1 Notation: two adjacent triangular elements 14

3.1 Example of set of plane-wave basis 20

4.1 Propagative wave benchmark with square domain: plane-wave basis 36
4.2 Propagative wave benchmark with square domain: plane-wave basis 37
4.3 Propagative wave benchmark with square domain: exact solution 38
4.4 Propagative wave benchmark with square boundary: relative L^2-error . . . 39
4.5 Propagative wave benchmark with square boundary: condition number . . 40
4.6 Propagative wave benchmark with square boundary: relative L^2-error . . . 41
4.7 Propagative wave benchmark with square boundary: relative L^2-error . . . 42
4.8 Propagative wave benchmark with square boundary: relative L^2-error . . . 43

5.1 Propagative wave benchmark with square boundary: structured mesh . . . 46
5.2 Propagative wave benchmark with square boundary and structured mesh: exact and numerical solution 47
5.3 Propagative wave benchmark with square boundary and structured mesh: numerical solution 47
5.4 Propagative wave benchmark with square boundary and structured mesh: condition number and relative L^2-error 48
5.5 Propagative wave benchmark with square boundary: unstructured mesh . . 49
5.6 Propagative wave benchmark with square boundary and unstructured mesh: numerical solution 50
5.7 Propagative wave benchmark with square boundary and unstructured mesh: condition number and relative L^2-error 50
5.8 Scattering benchmark with square boundary: mesh and exact solution . . . 51
5.9 Scattering benchmark with square boundary: $\imath\kappa$, numerical solution and error 52

5.10 Scattering benchmark with square boundary: sqrt, numerical solution and error 52
5.11 Scattering benchmark with square boundary: refinements 53
5.12 Scattering benchmark with square boundary: refinements 54
5.13 Scattering benchmark with square domain: error 55
5.14 Scattering benchmark with curved boundary: mesh and exact solution . . 56
5.15 Scattering benchmark with curved boundary: $\imath\kappa$, numerical solution and error 57
5.16 Scattering benchmark with curved boundary: sqrt, numerical solution and error 57
5.17 Scattering benchmark with curved boundary: refinements 58
5.18 Scattering benchmark with curved boundary: refinements 58
5.19 Scattering benchmark with curved boundary: $\imath\kappa$, numerical solution and error 59
5.20 Scattering benchmark with curved boundary: sqrt, numerical solution and error 59
5.21 Scattering benchmark with aircraft: numerical solution 60
5.22 Scattering benchmark with two fissures: numerical solution 61

Acknowledgements

I take these last pages as an opportunity to thank all the people without whom I would not have been able to complete my master's thesis in the best possible way.

I am grateful for all my advisors that helped me throughout the development of the project and the writing process of the thesis: Prof. Paola Francesca Antonietti for carefully following my work and supporting me, Dr. Axel Modave for his constant availability and huge patience in transmitting to me a part of his knowledge whenever I encountered issues and scenarios that I found hard to understand and Prof. Gwénaël Gabard for enlightening and enriching our discussions each time with new effective ideas and original points of view.

I do find straightforward conceiving this moment as a natural way to reflect not only on the last year during which I have been working on my thesis since it represents just the final step of a much longer journey that I started almost six years ago with the beginning of my university career. Therefore, I am going to quickly trace back the time and acknowledge all the people whose support, presence and love have turned out to be crucial and fundamental for the conclusion of this path.

First of all, my family deserves a special recognition for always being there supporting my choices and ideas and for making available a safe environment filled with unconditional love in which I have been able to freely express. I hope I made them all proud of the man I have eventually become.

Kevin and Camilla have constantly been pushing me to look at situations with a different angle and under an original perspective which has made it extremely easy to spot the light in dark corners. I am grateful for their teaching and genuine love.

Caterina and Giulia made *La signora in giallo* and our friendship a solid column whose stability and protection have always been something I could rely on inside and, most importantly, outside the walls of the university. I will always be there for you as I know you will for me.

Paolo, Francesco and Lupo have been and still represent huge sources of inspiration and examples of wonderful and dedicated people I have been glad to share my path with and who I know I will be able to count on forever.

Micol and Maddalena, with their spontaneity and irrepressible sympathy, created indelible memories that I jealously keep in mind and a safe bubble in which I can take refuge whenever pressure and hard times seem too hard to handle.

Elitsa, Sasha, Daniel and Sari have been essential since I moved to Paris almost two years ago and I owe them one of the most important lessons I have learnt so far: home is where the heart is. Thanks to all of them for being inspirational with their personal stories and silently helping me building a new secure place far from Italy.

Lastly, I want to conclude by spending few words about myself. Besides the academic obstacles that I had to face (*e.g.* Gram-Schmidt theorem, distributions), many more and harsher regarding my personal life arose. Being a very private person, most of the times I felt more comfortable to deal with them on my own. The common thread has always been my fright and when I had to stand in front of it I felt vulnerable and helpless. However, those moments forced me to seek the light, discover myself and eventually survive.

I still have fears and there are still things that I am scared of, but now I am supported by a new consciousness that makes me aware of my limits, capacities and strengths. This is the power I do have faith in, that I will never stop to rely on and that allows me to constantly grow, evolve and *metamorphose*.

I dedicate this moment to the man who now stares at his fears with a smile.

Take the pain and turn it into art
Metamorphose

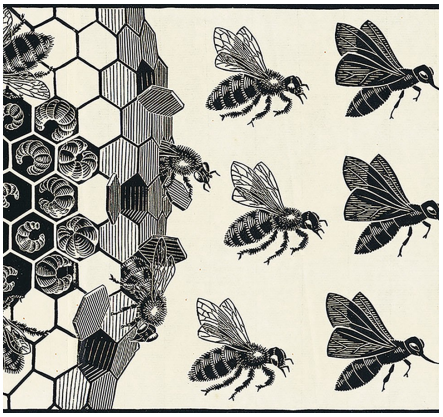

M.C. Escher. *Metamorphosis III*. 1968, woodcut, Escher in Het Paleis, The Hague.
https://noproscenium.com/nyc-escher-the-exhibition-experience-3275d5699bbd